# Trans-collicular pathways for sensory-motor integration in the whisker system

Jesús Martín-Cortecero [a,1,*], Emilio Ulises Isaías-Camacho[a,1], Berin Boztepe[a,b,1], Katharina Ziegler [a], Rebecca Audrey Mease[a] and Alexander Groh [a,*]

[a] Medical Biophysics, Institute for Physiology and Pathophysiology, Heidelberg University, 69120, Germany.
[b] Current affiliation: Neuroradiology Department, University Hospital Heidelberg, 69120 Heidelberg, Germany
[1] JMC, EIC, and BB contributed equally to this work
[*] To whom correspondence may be addressed. Email: martin-cortecero@physiologie.uni-heidelberg.de; groh@uni-heidelberg.de

## Summary

Most brain circuits comprise intermingled neuronal populations with heterogeneous input and output connectivity, which limits the ability to unambiguously map how the circuit of interest synaptically links specific input pathways to specific downstream targets. By applying newly available transsynaptic and intersectional tracing tools to investigate input-output connectivity of the superior colliculus (SC), a conserved midbrain-node with extensive long-range connectivity throughout the brain, we identify hitherto unknown connectivity features underlying cortical control of SC sensory-motor transformations. We pinpoint a whisker region in the SC of mice as a node for the integration of somatosensory and motor cortical signals. Tracing input-defined pathways from brainstem, motor- and somatosensory cortices to the whisker SC and further on to collicular downstream targets in the midbrain and brainstem revealed that long-range inputs establish synaptic contacts with inhibitory and excitatory SC-output neurons, thereby providing monosynaptic trans-collicular pathways between specific cortical and subcortical circuits for somato-motor integration.

**Keywords:** transsynaptic; trans-collicular; superior colliculus; sensorimotor convergence; long-range GABA projections

## Highlights

- Transsynaptic and intersectional tools uncover hitherto unknown but prevalent connectivity motifs of the superior colliculus (SC).
- Motor- and somatosensory cortex link to brainstem and diencephalon circuits via monosynaptic trans-collicular pathways.

- Motor- and somatosensory cortex convergence in a subpopulation of SC neurons.
- Cortical and brainstem pathways innervate long-range GABAergic neurons in SC, which project to higher-order thalamus and the zona incerta.

## Introduction

The superior colliculus (SC) is part of a phylogenetically ancient brain network that directs quick motor actions in response to ascending sensory signals (Basso et al., 2021; Corneil and Munoz, 2014). These sensory-motor transformations are thought to be modulated by cortical inputs impinging onto SC circuits (Benavidez et al., 2021; Liu et al., 2022; Zingg et al., 2017). However, the sparsity of microanatomical data on the input-output organization of the SC – particularly how specific input pathways map to specific SC downstream targets – imposes a bottleneck on our understanding of the descending cortical control of SC-generated behaviors.

Considering the diverse and dense connectivity of the SC with the majority of the neural axis, relatively few studies have delineated the precise input-output connectivity of defined subpopulations in SC (Basso et al., 2021). Recent large-scale mapping efforts of cortico-collicular pathways systematically identified cortical axonal target zones in the SC from which anterograde projection maps were created (Benavidez et al., 2021). This approach has been successfully used to tile the SC into input zones and subsequently chart zonal downstream targets. However, in light of the established role of the SC as an integrator of multi-modal input from several converging pathways (Meredith and Stein, 1986; Wallace et al., 1993), bulk approaches unavoidably label mixed SC populations with heterogeneous input profiles, e.g. retinal and cortical inputs (Kitanishi et al., 2022) and therefore limit the ability to unambiguously link specific input pathways to specific SC downstream targets. Indeed, input-output connectivity via the SC is mostly considered at the level of SC layers (Liu et al., 2022), due to the lack of adequate tools to assess connectivity at the granularity of input-defined cell types.

However, such precise knowledge about pathway-specific connectivity features of the SC is necessary to determine how cortico-collicular pathways act on downstream target circuits. Cortical influence may be indirect, via multi-synaptic intra-collicular circuits, or conversely, more direct via putative ‘trans-collicular’ pathways in which SC input neurons targeted by corticocolicular projections also monosynaptically connect to downstream targets. Identifying such trans-collicular pathways linking cortex and SC downstream targets would advance our understanding of cortical modulation of SC-mediated behaviors (Basso et al., 2021; Chou et al., 2018; Liang et al., 2015; Shang et al., 2019), particularly in the context of growing efforts

to study SC circuits in neuropsychological disorders (Baek et al., 2019; Bogadhi et al., 2019; Nyffeler et al., 2021).

The highly multisensory nature of the SC has motivated a large body of studies addressing integration of visual, auditory, somatosensory, and motor signals in the SC (Bezdudnaya and Castro-Alamancos, 2011, 2014; Castro-Alamancos and Favero, 2016; Duan et al., 2021; Gharaei et al., 2018; Meredith and Stein, 1986; Wallace et al., 1993). Direct anatomical demonstrations of long-range input convergence on the level of individual SC neurons have been challenging and have only recently been accomplished for sensory pathway convergence (Kitanishi et al., 2022), however whether sensory and motor pathways converge in individual SC neurons is as of yet unknown, despite the pivotal functional relevance of such a connectivity scheme.

Moreover, how cortical long-range projections engage specific excitatory or inhibitory SC microcircuits is largely unknown, despite the decisive impact such circuits could have on top-down modulation of SC-mediated innate escape and defense behaviors (Li et al., 2021; Liang et al., 2015; Zingg et al., 2017). Although the SC comprises diverse excitatory and inhibitory neuronal cell types – approximately one third of visual SC neurons are GABAergic (Liu et al., 2022; Whyland et al., 2020) – to what degree cortico-tectal pathways directly recruit inhibitory SC-circuits is only beginning to be understood (Duan et al., 2021)

Here, we investigate the input-output connectivity of the mouse lateral SC which is involved in the processing of whisker information (Bezdudnaya and Castro-Alamancos, 2011; Castro-Alamancos and Favero, 2016) – a primary sense for rodents and other animals (Brecht et al., 2011; Catania et al., 2008; Muthuramalingam and Bruecker, 2019; Petersen, 2019). Using transsynaptic tracing, intersectional viral approaches, and *in vivo* electrophysiology in combination with optogenetics, we investigated the microanatomical architecture of the lateral SC and addressed putative direct trans-collicular links between long-range inputs and long-range outputs. By labeling input-defined SC neurons and tracing their axonal outputs to downstream targets, we revealed direct trans-collicular pathways linking cortical and subcortical whisker-related circuits to multiple diencephalic and brainstem nuclei as trans-collicular target structures. Furthermore, transsynaptic labeling in combination with optogenetic input mapping revealed long-range input convergence on the level of individual SC neurons, with approximately one third of the cortical recipient SC neurons receiving convergent input from both motor and barrel cortex. Long-range input pathways targeted inhibitory SC neurons projecting to the zona incerta, suggesting trans-collicular circuits for cortical disinhibition of higher-order thalamus. Together this study pinpoints a ‘whisker SC’, in

which converging cortical and trigeminal inputs innervate GABAergic and non-GABAergic SC neurons, which in turn provide trans-collicular pathways to downstream whisker circuits in the diencephalon and brainstem.

## Results

**Input pathways to the lateral superior colliculus from motor- and somatosensory cortex and the trigeminal complex.**

First, to identify whisker-related projections to the SC (SC-projecting neurons) we injected retrograde rAAV-tdTomato in lateral SC (LSC) (Fig. 1A). Retrogradely labeled SC-projecting neurons were found in multiple cortical and subcortical areas (Fig. 1B), including whisker-related areas (Fig. 1C, D) in the ipsilateral barrel cortex (BC) and whisker motor cortex (Sreenivasan et al., 2016), (MC: M1 & M2, Supplementary Fig. S1), and in the contralateral trigeminal complex in the brainstem (Bs, Fig. 1E). In addition to the whisker-related projections to SC, we found retrogradely-labeled neurons projecting to the LSC in the auditory, insular- and ectorhinal cortices (Benavidez et al., 2021).

Analysis of the laminar profile of SC-projecting neurons in MC and BC revealed that cortico-collicular neurons originate in layer 5 (L5) in both cortices (Fig 1C, D). We further confirmed the L5 origin of cortico-collicular projections by registering SC-projecting somata with layer 6 (L6)-specific EYFP fluorescence in an Ntsr1-EYFP reporter mouse line, showing segregation of these two subcortical projection neuron types (Fig. 1C). Moreover, virus-mediated labeling of cortical boutons revealed dense innervation of LSC by MC and BC, with moderately sized cortico-collicular boutons (median diameters: BC 1.15 µm, MC 1.38 µm, Supplementary Fig. S2), consistent with recent reports (Prasad et al., 2020; Rojas-Piloni et al., 2017). Thus, the LSC receives direct and dense input from whisker areas in the brainstem and from L5 neurons in the barrel- and motor cortices.

**A** Retrograde labeling of SC projecting neurons

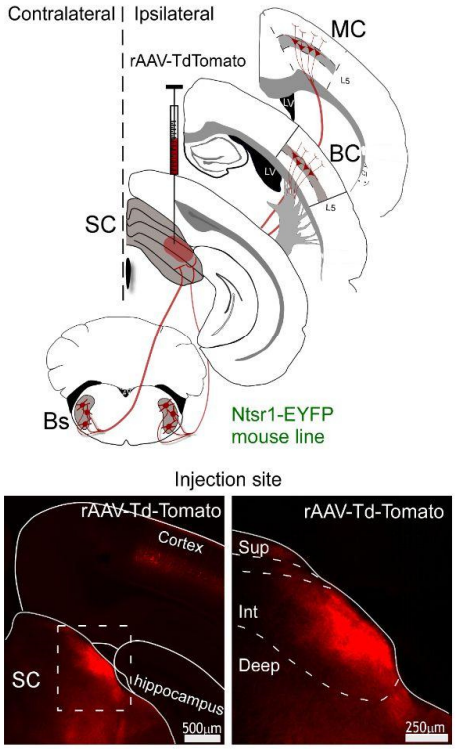


**B** LSC Projecting sites

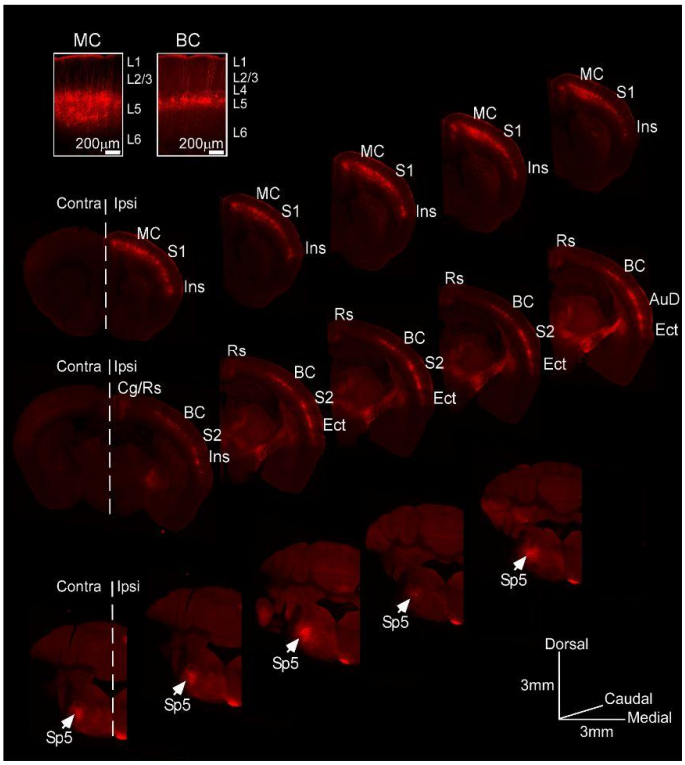


**C** Cortico-collicular neurons

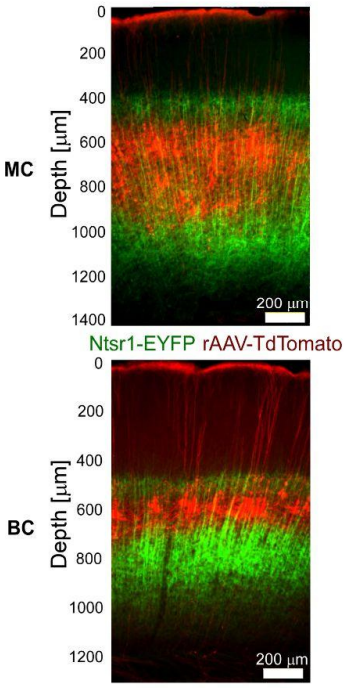


**D** Laminar profile of cortico-collicular neurons

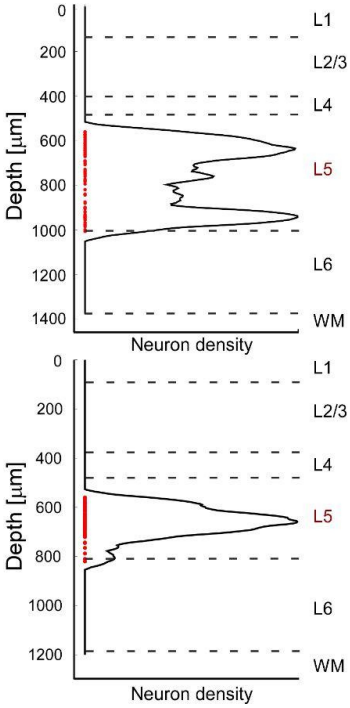


**E** Trigemino-collicular neurons

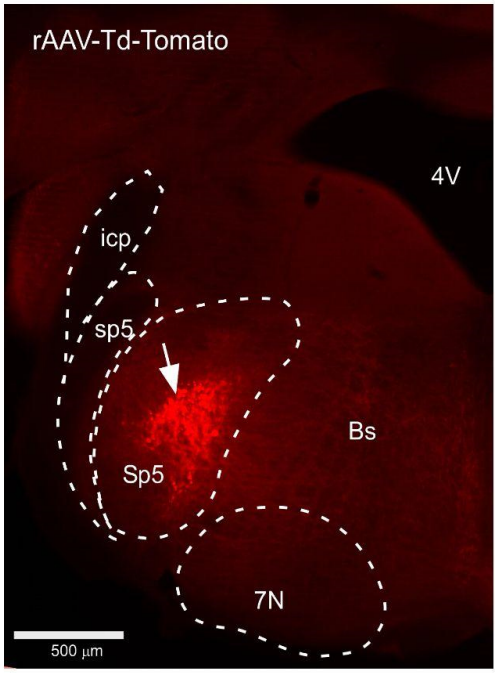

**Fig. 1. Lateral superior colliculus is a common target of projections from whisker-related cortical and brainstem regions.**

*(A)* Upper: Retrograde viral labeling of LSC-projecting neurons: rAAV-tdTomato (red) injection into LSC (Ntsr1-ChR2-EYFP mouse line). Lower: Example images of injection site in LSC showing td-Tomato expression (red).
*(B)* Consecutive fluorescent images (rostral to caudal) showing labeled LSC-projection areas throughout the brain, including ipsilateral MC and BC, and contralateral Sp5 in the trigeminal complex. Insets show L5 neurons in MC and BC at higher magnification. Abbreviations: AuD, auditory cortex; BC, barrel cortex; Cg, cingulate cortex; Ect, ectorhinal cortex; Ins, insular cortex; MC, motor cortex; Rs, retrosplenial cortex; S1, primary somatosensory cortex; S2, secondary somatosensory cortex; Sp5, spinal trigeminal nucleus.
*(C)* Fluorescence images of MC and BC (coronal slices) showing LSC-projecting neurons in layer 5 (red, TdTomato) relative to genetically identified layer 6 neurons (green, Ntsr1-EYFP line).
*(D)* Depth and laminar distributions of LSC-projecting neurons in MC and BC. Red dots depict the soma depths of LSC-projecting neurons (relative to pia = 0 µm, MC: median depth -741, IQR = 272 µm; BC: median depth = -648, IQR = 71 µm,). Depth-resolved soma densities (black solid lines) are shown relative to layer borders and white matter (WM) (dashed horizontal lines, estimated based on DAPI signals).
*(E)* LSC-projecting neurons (red, Td-Tomato) in the contralateral brainstem are located in the spinal trigeminal nucleus (Sp5). Abbreviations: 4V, fourth ventricle; icp, inferior cerebellar peduncle; sp5, spinal trigeminal tract; Sp5, spinal trigeminal nucleus; Bs, brainstem; 7N, facial nucleus.
Exact N in Supplementary Table S2.

**Cellular organization of somatosensory and motor pathways in the lateral SC.**

The retrograde virus experiments (Fig. 1) suggest that the lateral SC integrates whisker-related long-range input from MC, BC, and Bs, and is therefore a potential node for whisker signal integration in the midbrain. However, it is not known to which degree these input pathways converge within the LSC. To address how these long-range input pathways are organized within LSC, we transsynaptically labeled MC-, BC-, and Bs-recipient neurons (RNs) in SC and compared their relative distributions. After injecting cocktails of AAV1-Cre + AAV2-DIO-mCherry into MC, BC, and Bs, and AAV2-DIO-EGFP in SC (Fig. 2A), transsynaptically labeled populations of RNs were readily visible in the intermediate layers of SC by their fluorescence (Fig. 2B, Supplementary Fig. S3). This allowed us to reconstruct the three RN populations (MC-RNs, 6 mice; BC-RNs, 6 mice; Bs-RNs, 7 mice) and register them to standard anatomical borders within SC, revealing the intermediate layer of the LSC (Fig. 2C) as a discrete point of convergence for all three whisker-related input pathways. The RNs' distributions largely overlapped along the antero-posterior axis, although MC-RNs showed a slight anterior bias relative to BC-RNs and Bs-RNs (Fig. 2D). The marked overlap between recipient zones suggests an anatomical substrate for possible integration of long-range inputs at a cellular level.

We next compared the RN zones in the dorsal-ventral and medial-lateral dimensions by registering fluorescence- thresholded representative slices for each RN population at a similar

anterior-posterior coordinate. We found distinct but overlapping RN zones: a medial cortical-recipient zone with considerable overlap between MC- and BC-RNs and a ventral-lateral Bs-recipient zone (Fig. 2E). Indeed, labeling cortical (MC + BC) RNs with mCherry and brainstem RNs with EGFP confirmed a modest topographic segregation (Fig. 2F) such that cortical RNs (median = 1115 μm) were located dorsal to Bs-RNs (median = 1365 μm) in the intermediate layer of LSC.

Together, the anterograde and retrograde tracing experiments identify a region within the intermediate layers of the LSC which spans approximately 1.2 mm in the anterior-posterior axis and is targeted by several long-range whisker-related inputs as well as by other inputs from the auditory, insular, and ectorhinal cortices. To assess whether this anatomically defined whisker SC indeed encodes whisker signals, we made silicon probe recordings of single unit activity in the LSC in anesthetized animals and found robust, short-latency responses to whisker stimulation in this area (Supplementary Fig. S4). Analogous to the superficial layers of SC, which are frequently referred to as ‘visual’ (Basso et al., 2021; Robinson and McClurkin, 1989), our results suggest a ‘whisker’ SC region in the mouse, located ventral to the visual SC.

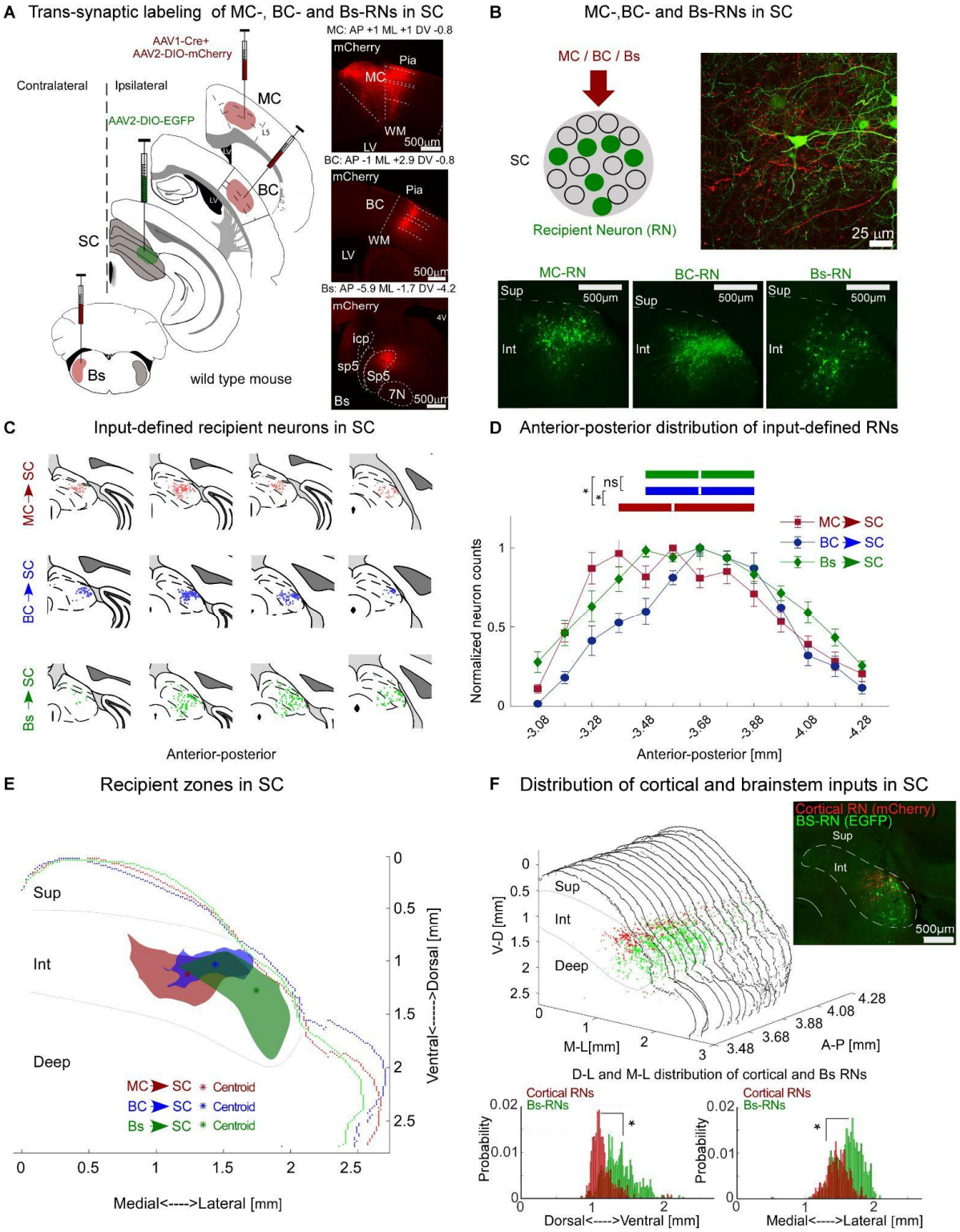


**Fig. 2. Whisker-related sensory-motor recipient neurons in overlapping subzones of the intermediate layer LSC.**

(*A*) Schematic of transsynaptic labeling of MC-, BC- and Bs-RNs in SC (left). Cocktails of AAV1-Cre + AAV-DIO-mCherry were injected into projecting sites (MC, BC, or Bs) and AAV2-DIO-EGFP in SC. Example fluorescent pictures (right) of mCherry expression (red) in the projecting sites. Abbreviations: LV, lateral ventricle; icp, inferior cerebellar peduncle; Pia, pia mater; sp5, spinal trigeminal tract; Sp5, spinal trigeminal nucleus; WM, white matter; 7N, facial nucleus.

(*B*) Top left: Schematic of transsynaptically labeled RNs (green). Top right: Example confocal image of SC showing mCherry-expressing BC axons (red) and Cre-dependent expression of EGFP in BC-RNs (green). Bottom: Fluorescent images of EGFP expression (green) in MC-, BC- and Bs- RNs.
(*C*) Example reconstructions of the three RN populations along the anterior-posterior axis (red: MC-RNs; blue: BC-RNs; green: Bs-RNs), registered to standard anatomical borders within SC.
(*D*) Anterior-posterior distributions of RNs. Data points show mean RN counts per 100 µm bin (red: MC-RNs, 6 mice; blue: BC-RNs, 6 mice; green: Bs-RNs,7 mice) normalized to their maximum count. Box plots show medians and IQRs in mm, ([median, Q1, Q3 in mm] MC-RNs: 3.58, 3.38, 3.88; BC-RNs: 3.68, 3.48, 3.88; Bs-RNs: 3.68, 3.48, 3.88; Kruskal-Wallis, $p < 0.01$).
(*E*) Comparison of recipient zones in the dorsal-ventral (DV) and medial-lateral (ML) dimensions in SC. Fluorescent thresholded representative slices of each RN population, registered at a similar AP coordinate. (Centroids: [DV, ML, µm] MC: 1123, 1505; BC: 1035, 1297; Bs: 1276, 993).
(*F*) Co-labeling experiment of cortical (red, MC-RNs + BC-RNs) and Bs-RNs (green). Top right: example fluorescent single image showing cortical and peripheral RNs. Middle: fluorescence thresholded RN signals from 15 consecutive images. Bottom: Histograms show the thresholded pixel gray value probability for cortical-RNs and Bs-RNs in the DV axis and in the ML axis
([DV, median and IQR, relative to SC dorsal surface] Cortical-RN [µm]: 1115, 147; Bs-RN: 1365, 281, Wilcoxon <0.001; [ML, median and IQR, µm relative to SC midline] Cortical-RN: 1472, 211; Bs-RN: 1637, 287, $p < 0.001$).

* represents $p < 0.01$; D: Kruskal-Wallis, F: Wilcoxon rank-sum; exact p values in Supplementary Table S1, exact N in Supplementary Table S2. Data are shown as mean ± S.E.M.

**Cortico- and trigemino-collicular pathways directly target GABAergic neurons in lateral SC.**

The previous results provide anatomical evidence for whisker-related recipient neurons in the LSC which are organized into input-defined recipient subzones. Since the SC is composed of excitatory and inhibitory neurons (Liu et al., 2022; Whyland et al., 2020), it is of important functional relevance whether and to what extent long-range inputs from MC, BC, and Bs directly target GABAergic neurons.

To test for monosynaptic innervation of GABAergic SC neurons, we employed a transsynaptic intersectional strategy that allowed us to separate inhibitory recipient neurons (iRNs) from the population of RNs for each of the three investigated long-range pathways. Injecting GAD-Cre mice, which express Cre in GABAergic neurons (Melzer et al., 2012), with anterograde virus (AAV1-Flpo) into MC, BC or Bs and conditional reporter viruses (AAV-ConFon, AAV-fDIO) into LSC allowed us to differentially label RNs with mCherry and iRNs with EYFP in the same mice (Fig. 3A, B, see Supplementary Methods and Supplementary Figs. S5, 6 for controls).

Reconstructions of the fluorescently labeled RN and iRN populations readily show that iRNs are intermingled with RNs for all three input pathways (Fig. 3C, D). Moreover, this qualitative assessment suggests that all three input pathways directly target a considerable fraction of GABAergic neurons. Indeed, quantifying the iRN/RN proportions revealed that all pathways

similarly target approximately 34-37% GABAergic neurons along the full extent of the recipient antero-posterior axis (Fig. 3E-G).

Do long-range inputs to LSC preferentially target inhibitory neurons? To quantify this directly, we first determined the proportion of GABAergic neurons (iNs) in the LSC and then compared iN proportions to iRN proportions. Using a GAD-GFP mouse line, in which GABAergic neurons are labeled with GFP, we additionally labeled all neurons using the pan-neuronal marker NeuN-Alexa 647 (Fig. 3E) and found that on average approximately 23% of the LSC neurons in the intermediate layer are iNs (Fig. 3F and Supplementary Fig. S7), lower than the 30% previously reported for the superficial SC (Liu et al., 2022). This higher proportion of iRNs compared to iNs (>34% vs 23%) suggests a targeting bias of long-range inputs towards GABAergic neurons, and furthermore suggests that the recruitment of GABAergic SC neurons by cortical and brainstem long-range input pathways is an essential component of whisker processing in the LSC.

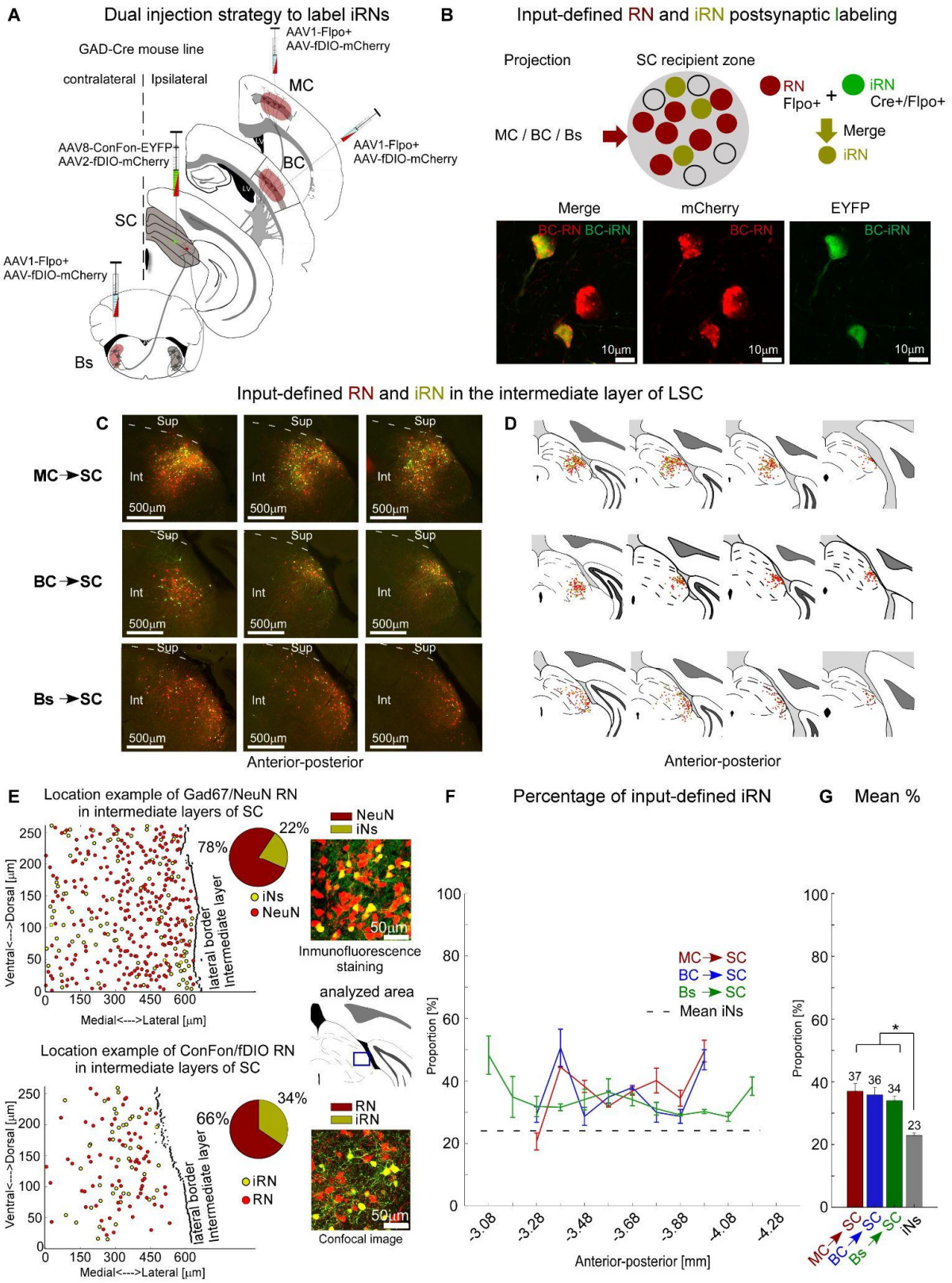


**Fig. 3. Cortico- and trigemino-collicular pathways directly target GABAergic neurons in LSC.**

(*A*) Schematic of dual injection strategy to label iRNs for each pathway. AAV1-Flpo + AAV-fDIO-mCherry was injected in the projecting sites (MC, BC, and Bs), and AAV8-Con/Fon-EYFP + AAV2-fDIO-mCherry in LSC of GAD-Cre mice to label iRNs and RNs respectively.

(*B*) Top: Schematic of transsynaptically labeled RNs (red) and iRNs (green). Bottom: Confocal images showing examples BC-iRNs and BC-RNs.

(*C)* Example fluorescence images showing iRNs and RNs in different AP sections of SC for MC, BC, and Bs pathways. Abbreviations: Int, Intermediate layers; Sup, Superficial layers.
*(D*) Example reconstructions of MC-, BC- and Bs-iRN and RN populations along the anterior-posterior axis (red: RNs, yellow: iRNs), registered to standard anatomical borders within SC.
(*E*) Top: Quantification of iNs (yellow) and NeuN-labeled SC neurons (red) in the GAD-GFP mouse line. Shown is an example reconstruction from one anterior-posterior section. Pie chart shows iNs/NeuN proportions (84 iNs/384 NeuNs, 22%) and confocal image shows example fluorescent data. Bottom: same as Top but for quantification of iRN/RN ratios (41 iRNs and 119 RNs, 34%) from a MC-iRN / RN experiment.
(*F*) Population analysis of the proportions of iRN/RN for each whisker-related input pathway (colored lines) along the anterior-posterior SC axis and iNs/NeuN proportion (dashed line).
(*G*) Means and SEMs of proportions of iNs/NeuN (gray) and iRN/RN for each input pathway (MC in red, BC in blue, Bs in green): [mean per slice ± SEM, iRN/RN or iNs/NeuN, n mice]; MC: 36.4 ±2.4%, 2; BC: 35.6 ±2.4%, 3; Bs: 33.2 ±1.5%, 3; iNs/NeuN: 23.1%± 1.2, 1). * represents $p < 0.01$; Kruskal-Wallis; exact p values in Supplementary Table S1, exact N values in Supplementary Table S2. Data are shown as mean ± S.E.M.

**Somatosensory and motor pathways convergence in the lateral SC.**

Our analysis of the topographic organization of the different RN populations (Fig. 2) showed considerable overlap between recipient zones in LSC, suggesting possible convergence of long-range input pathways on the level of individual SC neurons. To address whether single LSC neurons indeed receive monosynaptic input from two input pathways, we identified those RNs with convergent input (CVG-RN) using an intersectional strategy as follows: in the same mouse, we injected two projection sites – e.g. MC and BC – each with a different transsynaptic variant – AAV1-Cre or Flpo. Indeed, injections of the double-conditional (Cre- and Flpo-dependent) reporter virus in SC revealed CVG-RNs (4 MC & BC, 3 MC & Bs, and 2 BC & Bs mice, Fig. 4A, B). Comparing the distributions of the three CVG-RN populations (BC & Bs, MC & Bs, and MC & BC CVG-RN, Fig. 4C) along the anterior-posterior SC axis revealed that the MC & Bs CVG-RNs population was anteriorly skewed, while both MC & BC, and BC & Bs CVG-RN populations were skewed more posteriorly ($p < 0.001$, Fig. 4C).

These results demonstrate convergence of long-range input pathways in a subpopulation of convergence neurons in the whisker SC, raising the question of the relative degree of convergence between pairs of input pathways. We therefore compared (1.) z-scored mean CVG-RN counts per input pair and (2.) the proportion of CVG-RNs with respect to RNs between all input pairs. These analyses revealed that MC & BC convergence stands out compared to the other convergence pairs. Notably, the z-scored MC & BC CVG-RN counts (4 mice) showed a 2.33-fold higher deviation compared to Bs & cortex convergence (5 mice, Fig. 4D).

To calculate the proportions of CVG-RNs with respect to RNs (i.e. the proportion of convergence neurons relative to all recipient neurons) for each convergence pair, we counted

mCherry labeled RNs and EYFP-labeled CVG-RNs (Fig. 4A and Supplementary Methods) and compared these proportions among the three input pairs. We found that for the MC & BC input pair, about 23% of the neurons are convergence neurons, while for the BC & Bs and MC & Bs pairs, only about 10% are convergence neurons (Fig. 4E). Thus, regardless of cortical projection origin, mean cortico-cortical convergence is about 2.3-fold higher than brainstem-cortical convergence. Finally, to estimate the location of the convergence zone between motor- and barrel cortices in the whisker SC in coordinate space, we registered the coordinates of MC & BC CVG-RNs (222 neurons) and fitted a two-component Gaussian Mixture Model, showing that the MC & BC CVG-RNs were predominantly found in the dorsal portion of the intermediate layer (Fig. 4F).

The finding of cellular convergence of long-range input pathways in the SC and the relative abundance of MC-BC convergence highlights the whisker SC as a node for the integration of somatosensory and motor cortical signals. This convergence motif could potentially support fast, temporally precise integration of signals from different cortical regions, and we next tested this possibility at the functional level.

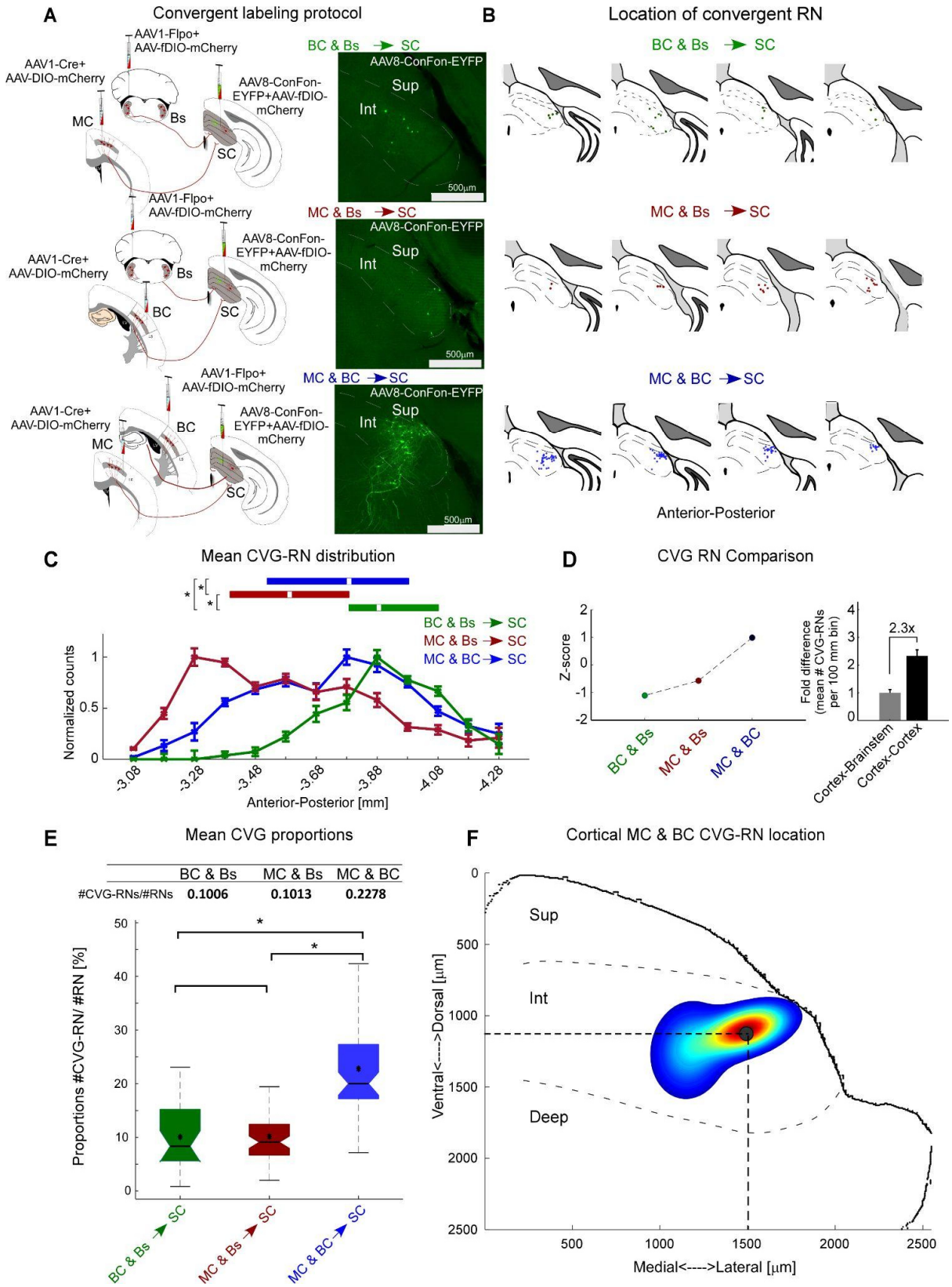


**Fig. 4. Whisker-related input pathways converge in subpopulations of LSC neurons.**

(*A*) Left: Schematic of convergence labeling protocol to identify different RN and CVG-RN populations in SC (MC & BC, MC & Bs, and BC & Bs). AAV1-Cre + AAV2-DIO-mCherry and AAV1-Flpo + fDIO-mCherry were injected into two different projecting sites and AAV8-Con/Fon-EYFP + AAV2-DIO-

mCherry into LSC to reveal CVG-RNs and RNs. Right: Example fluorescent images showing CVG-RNs in intermediate layers (Int) of SC.
(*B*) Example reconstructions of CVG-RNs populations (green: BC & Bs; red: MC & Bs; blue: MC & BC) along the anterior-posterior axis, registered to standard anatomical borders within SC.
(C) Normalized distributions of CVG-RNs populations (green: BC & Bs; red: MC & Bs; blue: MC & BC) along the anterior-posterior axis (bin size 100 µm).
(*D*) Left: Z-scored mean number of CVG-RNs for each input pair. Right: Fold difference between mean number of CVG-RNs per 100 µm bin for cortex-cortex (4 mice) and brainstem-cortex.
(*E*) Proportions of CVG-RNs to RNs. Proportions of CVG-RNs were calculated from an additional AAV2-DIO-mCherry injection in SC to reveal the RNs from the projecting region injected with AAV1-Cre. Box plots of CVG-RN proportions to RNs for each convergence input pair (asterisks show the mean) ([median, mean, IQR] MC & BC: 0.20, 0.22, 0.01; BC & Bs: 0.08, 0.01, 0.09; MC & Bs: 0.09, 0.01, 0.06).
(*F*) The two-component Gaussian Mixture Model shows the area of MC & BC convergence zone in the dorsal part of the intermediate layer of SC (11 slices, 2 mice). The black dot indicates the location of the highest probability of finding MC & BC CVG-RNs (1126 µm from SC surface and 1492 µm from the midline).

* represents $p < 0.01$; C, E: Kruskal-Wallis; exact p values in Supplementary Table S1, exact N in Supplementary Table S2. Data are shown as mean ± S.E.M.

**Single LSC units integrate sensory- and motor cortex inputs.**

To validate the anatomical finding of monosynaptic convergence of MC and BC in LSC on the functional level, we performed electrophysiological recordings in LSC in combination with optogenetic stimulation of L5 neurons in MC and BC in anesthetized mice. We used Rbp4-Cre-ChR2-EYFP mice (n = 4), in which L5 neurons express ChR2 (Lohse et al., 2021; Xiong et al., 2015) and successively stimulated MC-L5 and BC-L5 during the same experiment by using a movable fiber optic placed above the pial surface (Fig. 5A).

By characterizing the evoked spiking activity of individual SC units in response to successive optogenetic stimulation of L5 in MC or BC (Fig. 5B), we were able to identify thirty units that responded to either MC-L5 or BC-L5, from which nine responded to both (Fig. 5C). Unit spike latencies in response to optogenetic stimulation of L5 were approximately 9 - 12 ms (Fig. 5D, exact values in Supplementary Table S3), comparable to the latencies of optogenetically-evoked spiking in L5 and L5-innervated downstream neurons in the thalamus (Arenkiel et al., 2007; Mease et al., 2016) suggesting monosynaptic activation of a subset of LSC neurons via L5-SC synapses.

In summary, these functional data show that approximately 30% of the optogenetically driven LSC units are responsive to both MC-L5 and BC-L5 stimulation (Fig. 5E), in line with the anatomical observation of approximately 23% of MC & BC CVG-RNs. Together, these results

show that the LSC has a significant subpopulation of neurons which integrate mono-synaptic input from MC and BC.

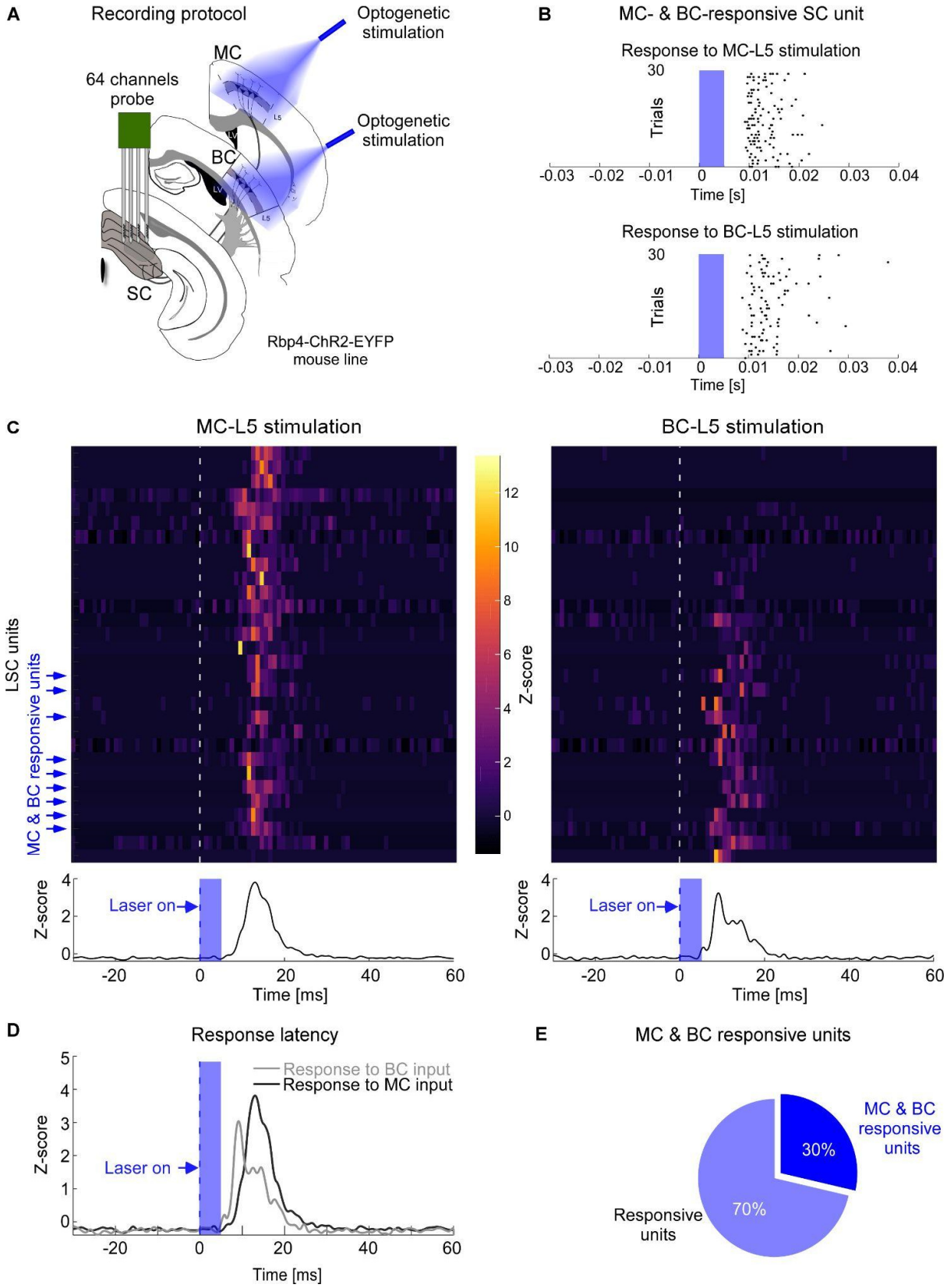

**Fig.5 MC and BC functional convergence in LSC.**

*(A)* Schematic illustrating the optogenetic stimulation of MC-L5 and BC-L5 and 64-channel silicon probe recording in LSC in Rbp4-Cre-ChR2-EYFP mice.
*(B)* Example raster plot of a single unit responding to both MC-L5 (top) and BC-L5 (bottom) laser stimulation (blue, 30 trials).
*(C)* Top: single unit PSTHs in response to MC-L5 (left) and BC-L5 (right) laser stimulation (dashed line). Units were ordered by responsive trial proportion to BC stimulation. Among 30 responsive units (out of 409 recorded SC units), 25 were responsive to optogenetic stimulation of MC-L5, 14 to BC-L5, and 9 to both MC-L5 and BC-L5 (blue arrows). Bottom: LSC population PSTHs for MC-L5 (left) and BC-L5 (right) laser stimulation (blue, laser on).
*(D)* Overlaid LSC population PSTHs for MC-L5 (black) and BC-L5 (gray) laser stimulation (blue).
*(E)* Proportions of MC-L5 or BC-L5 responsive units (blue) and units responding to both (dark blue).

See Supplementary Table S3 for extended data on unit population spiking characteristics.

**Trans-collicular pathways via cortico- and trigemino-collicular projections to the diencephalon and brainstem.**

The anatomical connections of the SC have been explored in great detail (reviewed in (Basso and May, 2017)), however, knowledge about the precise input/output relationships of individual input-defined SC neurons and the existence of direct trans-collicular pathways is lacking. Therefore, we employed the transsynaptic labeling approach to label RNs from all three input pathways as before. We noticed excellent labeling of RN axons, which allowed us to to trace input-defined axons to the brainstem and diencephalon (Fig. 6A, B, 3 mice). In the target nuclei, we observed axons and varicosities (Supplementary Fig. S8), suggesting that input-defined RN-projection neurons indeed form synaptic contacts with downstream target neurons.

We computed RN-output maps (see Methods) from reconstructed axon counts in order to estimate relative innervation strengths of the target nuclei (Fig. 6C, D), with values greater than or less than zero indicating relatively enriched or sparse innervation, respectively (Fig. 6C, D, right panels). All three trans-collicular pathways innervated multiple diencephalic nuclei, with the highest axonal density in zona incerta (ZI) and sensory-motor-related nuclei in the thalamus, i.e. the posterior- (PO), ventro-medial- (VM) and parafascicular (PF) nuclei. To a lesser extent, we found axons in the subthalamic- (STH), centro-medial-, centro-lateral-, precentral-, mediodorsal- (CM, CL, PC, MD), ethmoidal- (ETH), paraventricular- (PV), laterodorsal- (LD), rhomboid- and reuniens- (RH, Re) nuclei (Fig. 6A and C). Moreover, we found axons in the anterior pretectal area (APT), pre-rubral field and superior cerebellar peduncle (PR, SCP), the precommissural nucleus (PRC), and periaqueductal gray area (PAG).

In the brainstem, the highest relative axon counts were found in the caudal part of the pontine reticular- (PnC), the gigantocellular reticular- (Gi) and the facial nucleus (7N). To a lesser extent, we found axons in the principal trigeminal-(Pr5), spinal trigeminal-(Sp5), intermediate reticular-(iRT), dorsal periolivary region and the superior paraolivary-(DPO, SPO) and the ventral part of the pontine reticular-(PnV) nuclei (Fig. 6B, D). In general, the innervation strength of a given target was often similar for the three trans-collicular pathways, particularly brainstem targets. The output maps differed more strongly in the thalamus, for example one notable exception was the lateral-posterior nucleus (LP), which received relatively enriched innervation by Bs-RN axons.

Given the prevalence of inhibitory RN in LSC, we next investigated whether direct trans-collicular pathways extend to long-range GABAergic output. Surprisingly, we found that iRNs from all three pathways give rise to high density innervation of the ZI (Fig. 6E, Supplementary Fig. S9). To a lesser extent, we found iRN axons and varicosities in PO and PF. In contrast, no inhibitory projections were found in the brainstem. The results not only confirm connectivity between SC and the diencephalic and brainstem regions (White et al., 2004) but also reveal hitherto unknown trigeminal and cortical trans-collicular pathways with inhibitory functions in thalamic nuclei and the ZI. Moreover, based on the observed projection patterns, it would be expected that most of the RN and iRN innervate GABAergic neurons in dorsal and ventral ZI where the expression of GAD67 is predominant (http://www.brain-map.org), which may indicate a SC-mediated gate control mechanism of sensory-motor inputs to higher-order thalamus.

In summary, we found direct excitatory and inhibitory trans-collicular pathways – output pathways from input-defined RNs which bypass local processing in SC and preferentially target higher-order nuclei in the thalamus and the ZI. Furthermore, these findings suggest that higher-order nuclei in the thalamus – e.g. PO – which receive direct cortico-thalamic L5 input (Groh et al., 2008; Hoogland et al., 1987; Rojas-Piloni et al., 2014; Sumser et al., 2017) also receive indirect L5 information via cortico-collicular-thalamic pathways. These findings point to prevalent trans-collicular pathways that could rapidly route cortical and brainstem information to diverse points along the neural axis.

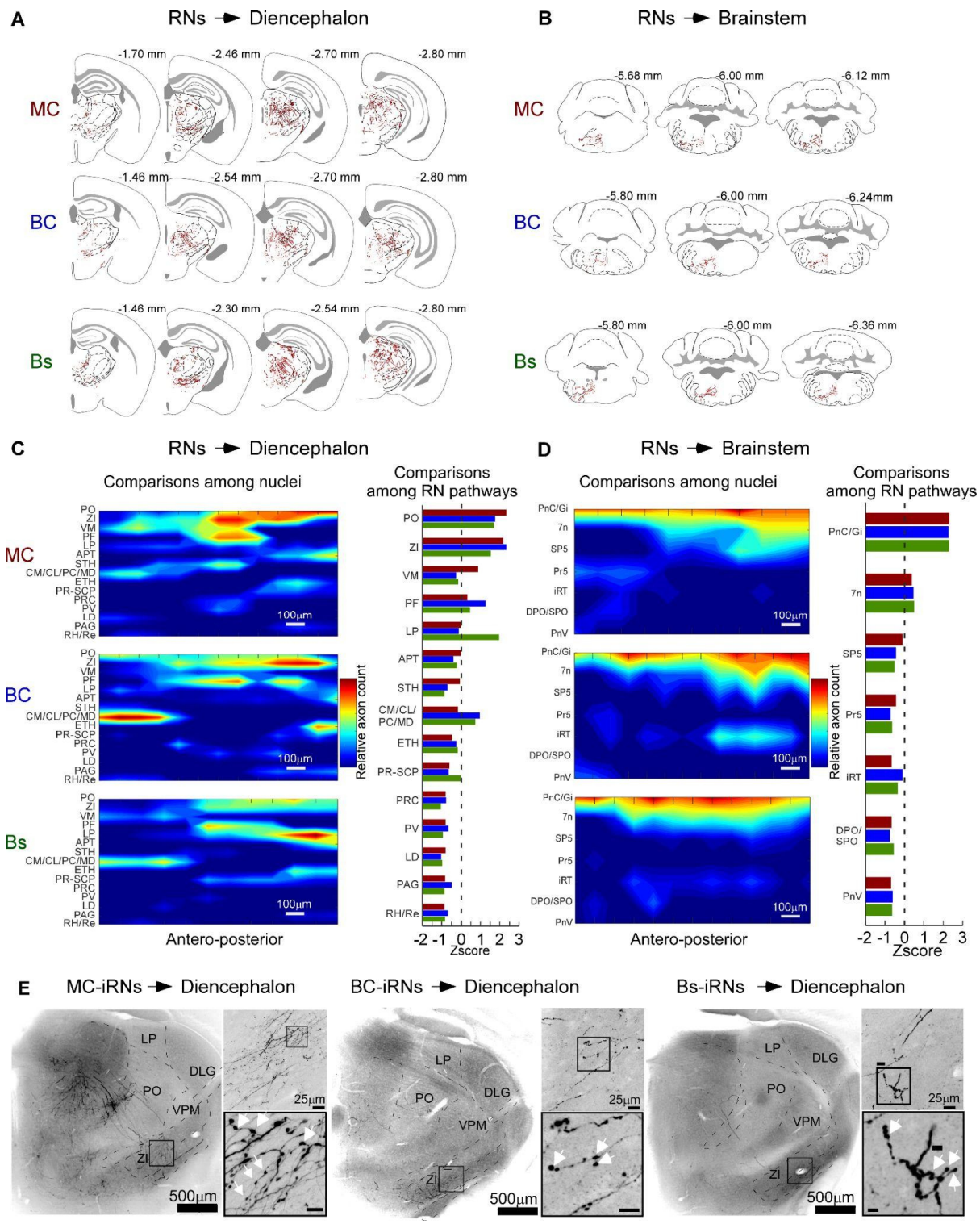


**Fig. 6. Axonal projections of cortico- and trigemino-collicular neurons to diencephalic and brainstem target nuclei.**

(*A*) Axon reconstructions of MC-, BC- and Bs-RNs in diencephalic nuclei in example sections along the AP axis.

(*B*) as (*A*) but in brainstem nuclei.

(*C*) Left panel: normalized relative axon counts (RAC) along the anterior-posterior axis in diencephalic nuclei from all three RN pathways. RAC values from blue to red: low to high. Right panel: Z-score normalization of the total number of axons per nucleus and comparison among RN-pathways (right

panel, 3 mice, diencephalic region 1.2 to 1.3 mm, brainstem region 1.1 to 1.4 mm, stippled line indicates Z-score = 0).
(D) same as (C) but for brainstem nuclei.
(E) Example confocal images (desaturated and inverted) of axons from MC-, BC- and Bs-iRN in the diencephalon. Inset images at a higher magnification show varicosities (white arrowheads, scale bar 5 µm).

## Discussion

*Trans-collicular pathways*

The superior colliculus – a highly conserved sensory-motor structure in vertebrates – is said to be one of the best-characterized structures in the brain (Basso and May, 2017; Basso et al., 2021; Liu et al., 2022). A large body of work revealed a complex long-range connectivity of the SC with the rest of the brain, comprising numerous cortical and subcortical input pathways and large numbers of target nuclei in the diencephalon and brainstem. However, addressing how particular input pathways connect to particular output targets via individual SC neurons has been challenging because of the lack of tools to determine the connectivity features of input-defined SC neurons. The present study analyzed the anatomical organization of the mouse LSC by employing transsynaptic viral approaches to trace input-defined pathways from the brainstem and motor and somatosensory cortices to the LSC, and further on to collicular downstream targets in the midbrain and brainstem. We identified a hitherto unknown but prevalent connectivity scheme: trans-collicular pathways, monosynaptically traversing through the LSC and linking cortical and trigeminal whisker circuits to downstream targets in the brainstem and diencephalon.

The anatomical and functional data suggest that the intermediate layers of the LSC serve as a main collicular whisker node. We found that the LSC is highly interconnected with whisker circuits throughout the brain, both in terms of inputs and outputs, in line with recent mapping efforts of the SC (Benavidez et al., 2021). Here, we were able to refine previous putative input-output maps by leveraging transsynaptic labeling to constrain the SC population of interest by upstream innervation source. For example, the present study shows that trans-collicular pathways from MC, BC and Bs avoid first-order thalamus, a finding with important functional relevance that could not be inferred from previous bulk labeling studies. Furthermore, we found that the LSC exhibits robust whisker encoding (Supplementary Fig. S4), in line with previous electrophysiological measurements in this area (Castro-Alamancos and Favero, 2016). In the context of whisking behavior, it is important to underline that long-range inputs from whisker-related areas to the LSC turn into direct outputs to the 7N, a brainstem motor-nucleus for whisker movements (Kleinfeld et al., 2006). Thus, while cortico-collicular pathways might modulate whisking behavior in a contextual manner, the trigemino-collicular pathway might be part of a sensory-motor loop (Kleinfeld et al., 2006) that could underlie the “minimal

impingement phenomenon", which rodents use to minimize the force of whiskers upon surface contact (Mitchinson et al., 2007). Notably, in the thalamus, the three investigated trans-collicular pathways originating in MC, BC and Bs target mostly high-order thalamic nuclei, such as PO, but not first-order thalamic nuclei. Thus, our viral transsynaptic tracing data suggests an indirect L5 trans-collicular pathway to PO in addition to the well-known direct cortico-thalamic pathway between cortical L5 neurons and PO (Groh et al., 2008; Hoogland et al., 1987; Rojas-Piloni et al., 2014; Sumser et al., 2017).

Importantly, we found that trans-collicular pathways include both GABAergic and non-GABAergic SC-projection neurons. Notably, GABAergic long-range projections target PO and the ZI but not – unlike non-GABAergic pathways – the brainstem. Thus, the PO and the ZI, the latter of which is a potent source of inhibition for high-order thalamic nuclei (Halassa and Acsady, 2016), receive both GABAergic and non-GABAergic trans-collicular input. Future investigations of how ZI integrates excitatory and inhibitory long-range inputs will likely generate substantial insight into modulation of ZI's myriad functions, which include locomotion, feeding, hunting, pain regulation, and defense behaviors (Chou et al., 2018; Shang et al., 2019). Given the largely inhibitory nature of the ZI, these hitherto unknown trigemino- and cortico-collicular long-range pathways with inhibitory functions in the ZI might be expected to disinhibit ZI's postsynaptic target regions.

Strikingly, we found that the whisker trigemino-collicular pathway sends abundant projections to the visual LP in the thalamus, providing an anatomical substrate for the recent findings that the LP integrates visual and tactile information (Petty et al., 2021). The integration of trans-collicular whisker signals in the LP may be an important mechanism underlying visuo-tactile functions such as hunting behavior, in which the SC has been shown to play a key role (Shang et al., 2019).

*Long-range input convergence in the LSC*

Despite the well-established multimodal nature of the SC and the abundance of input pathways targeting the SC, the question of parallel vs. convergent collicular pathways has been difficult to assess, in particular on a quantitative level. While functional observations of multisensory SC neurons (Wallace et al., 1993) consistently support convergence in the SC, only a few studies have directly investigated long-range convergence at the level of individual SC neurons using anatomical means (Feig and Harting, 1992; Hofbauer and Holländer, 1986; Kitanishi et al., 2022) and quantitative assessments of the level of convergence in the non-visual SC are missing. We used anatomical and functional tools to quantify the level of convergence of input pathways from MC, BC and Bs in individual SC neurons. For all tested

putative convergence pairs, we found subpopulations of recipient SC neurons, receiving monosynaptic input from two input pathways. The proportion of trigemino-cortical convergence LSC neurons receiving input from the brainstem and either of the cortical areas was approximately 10%. In contrast, the proportion of cortico-cortical convergence neurons (MC & BC) was more than twice as high (~23%). Probing individual LSC units for their responsiveness to consecutive optogenetic stimulation of layer 5 neurons in MC and BC revealed a similar proportion (~30%) of MC & BC convergence neurons in LSC.

While the exact functions of MC & BC convergence in SC remain to be elucidated, these sensory-motor convergence neurons could well contribute to the execution and control of motor plans (Duan et al., 2021). In this framework, inputs from MC inform the SC about an intended motor action i.e. an “efference copy” (Ford and Mathalon, 2019) of the motor command, while BC provides information on the resulting sensory status, thereby enabling mechanisms to initiate small motor command readjustments and/or context-dependent dampening or enhancement of sensation, possibly analogous to the SC mechanisms proposed for the stabilization of visual perception (Cavanaugh et al., 2016).

*Long-range innervation of GABA neurons in the LSC*

The SC contains a large fraction of GABAergic neurons, with proportions ranging from 30% to 45%, depending on the investigated species and region (Liu et al., 2022). Since the recruitment of GABAergic neurons likely plays critical roles in the regulation of SC functions, we investigated to what degree long-range inputs directly innervate SC-GABAergic neurons. We found that more than a third (34-37%) of MC-, BC- and Bs-targeted LSC neurons are GABAergic. This proportion significantly exceeded the fraction of GABAergic neurons in the LSC (~23%), suggesting an important functional role for the recruitment of inhibitory SC-circuits by cortical and trigeminal long-range inputs. Interestingly, a recent report using anterograde transsynaptic viral tracing found that nearly half of the SC neurons downstream of the secondary motor cortex are GABAergic (Duan et al., 2021). Together, these findings suggest that the dual recruitment of inhibitory and excitatory circuits in the SC provides long-range inputs, for instance cortico-collicular pathways, with the ability to flexibly dampen or enhance SC-mediated innate behaviors.

In summary, this study presents quantitative microanatomical evidence for hitherto unknown connectivity features of somato-motor pathways in the SC. In addition to sensory-motor convergence in the LSC, the results demonstrate that cortical and trigeminal inputs target GABAergic and non-GABAergic recipient neurons, which provide direct long-range output to diencephalic and brainstem nuclei involved in sensory-motor transformations.

## Acknowledgments

We thank Alexei Egorov (Heidelberg University) for helping with the rAAV-Td-Tomato experiments and Martha Bickford and her team (University of Louisville) for helping with the GABA immunolabeling. This work was funded through the DFG Grant GR3757/3-1, the Heidelberg Graduate Academy completion grant through the *Landesgraduiertenförderung* program with funds allocated by the German Ministry of Science, Research and Arts (EIC), the Chica and Heinz Schaller Stiftung (RM) and the Brigitte-Schlieben-Lange Programm by the Ministry of Science, Research and the Arts Baden-Württemberg (RM). We acknowledge the data storage service SDS@hd supported by the Ministry of Science, Research and the Arts Baden-Württemberg (MWK) and the German Research Foundation (DFG) through grant INST 35/1314-1 FUGG and INST 35/1503-1 FUGG. We also thank the Nikon Imaging Center at the University of Heidelberg.

## Author Contributions

J.M.C., E.I.C., B.B. and A.G. conceptualized the study; J.M.C., E.I.C., B.B., and K.Z. conducted anatomical research. J.M.C., E.I.C., conducted electrophysiological recordings. J.M.C., E.I.C. and B.B. conducted formal analysis; J.M.C., E.I.C., R.A.M and A.G. wrote the paper; J.M.C., E.I.C., K.Z., R.A.M and A.G. reviewed the paper.

## Declaration of interests

Authors declare that they have no competing interests.

## References


Arenkiel, B.R., Peca, J., Davison, I.G., Feliciano, C., Deisseroth, K., Augustine, G.J., Ehlers, M.D., and Feng, G. (2007). In vivo light-induced activation of neural circuitry in transgenic mice expressing channelrhodopsin-2. Neuron *54*, 205–218. .

Baek, J., Lee, S., Cho, T., Kim, S.-W., Kim, M., Yoon, Y., Kim, K.K., Byun, J., Kim, S.J., Jeong, J., et al. (2019). Neural circuits underlying a psychotherapeutic regimen for fear disorders. Nature *566*, 339–343. .

Basso, M.A., and May, P.J. (2017). Circuits for Action and Cognition: A View from the Superior Colliculus. Annu Rev Vis Sci *3*, 197–226. .

Basso, M.A., Bickford, M.E., and Cang, J. (2021). Unraveling circuits of visual perception and cognition through the superior colliculus. Neuron *109*, 918–937. .

Benavidez, N.L., Bienkowski, M.S., Zhu, M., Garcia, L.H., Fayzullina, M., Gao, L., Bowman, I., Gou, L., Khanjani, N., Cotter, K.R., et al. (2021). Organization of the inputs and outputs of the mouse superior colliculus. Nat. Commun. *12*, 1–20. .

Bezdudnaya, T., and Castro-Alamancos, M.A. (2011). Superior colliculus cells sensitive to active touch and texture during whisking. J. Neurophysiol. *106*, 332–346. .

Bezdudnaya, T., and Castro-Alamancos, M.A. (2014). Neuromodulation of whisking related neural activity in superior colliculus. J. Neurosci. *34*, 7683–7695. .

Bogadhi, A.R., Bollimunta, A., Leopold, D.A., and Krauzlis, R.J. (2019). Spatial Attention Deficits Are Causally Linked to an Area in Macaque Temporal Cortex. Curr. Biol. *29*, 726-736.e4. .

Brecht, M., Naumann, R., Anjum, F., Wolfe, J., Munz, M., Mende, C., and Roth-Alpermann, C. (2011). The neurobiology of Etruscan shrew active touch. Philos. Trans. R. Soc. Lond. B Biol. Sci. *366*, 3026–3036. .

Castro-Alamancos, M.A., and Favero, M. (2016). Whisker-related afferents in superior colliculus. J. Neurophysiol. *115*, 2265–2279. .

Catania, K.C., Hare, J.F., and Campbell, K.L. (2008). Water shrews detect movement, shape, and smell to find prey underwater. Proc. Natl. Acad. Sci. U. S. A. *105*, 571–576. .

Cavanaugh, J., Berman, R.A., Joiner, W.M., and Wurtz, R.H. (2016). Saccadic Corollary Discharge Underlies Stable Visual Perception. J. Neurosci. *36*, 31–42. .

Chou, X.-L., Wang, X., Zhang, Z.-G., Shen, L., Zingg, B., Huang, J., Zhong, W., Mesik, L., Zhang, L.I., and Tao, H.W. (2018). Inhibitory gain modulation of defense behaviors by zona incerta. Nat. Commun. *9*, 1151. .

Corneil, B.D., and Munoz, D.P. (2014). Overt responses during covert orienting. Neuron *82*, 1230–1243. .

Duan, C.A., Pan, Y., Ma, G., Zhou, T., Zhang, S., and Xu, N.-L. (2021). A cortico-collicular pathway for motor planning in a memory-dependent perceptual decision task. Nat. Commun. *12*, 2727. .

Feig, S., and Harting, J.K. (1992). Ultrastructural studies of the primate parabigeminal nucleus: electron microscopic autoradiographic analysis of the tectoparabigeminal projection in Galago crassicaudatus. Brain Res. *595*, 334–338. .

Fenno, L.E., Mattis, J., Ramakrishnan, C., Hyun, M., Lee, S.Y., He, M., Tucciarone, J., Selimbeyoglu, A., Berndt, A., Grosenick, L., et al. (2014). Targeting cells with single vectors using multiple-feature Boolean logic. Nat. Methods *11*, 763–772. .

Ford, J.M., and Mathalon, D.H. (2019). Efference Copy, Corollary Discharge, Predictive Coding, and Psychosis. Biol Psychiatry Cogn Neurosci Neuroimaging *4*, 764–767. .

Gharaei, S., Arabzadeh, E., and Solomon, S.G. (2018). Integration of visual and whisker signals in rat superior colliculus. Sci. Rep. *8*, 16445. .

Gong, S., Doughty, M., Harbaugh, C.R., Cummins, A., Hatten, M.E., Heintz, N., and Gerfen, C.R. (2007). Targeting Cre recombinase to specific neuron populations with bacterial artificial chromosome constructs. J. Neurosci. *27*, 9817–9823. .

Groh, A., de Kock, C.P.J., Wimmer, V.C., Sakmann, B., and Kuner, T. (2008). Driver or coincidence detector: modal switch of a corticothalamic giant synapse controlled by spontaneous activity and short-term depression. J. Neurosci. *28*, 9652–9663. .

Halassa, M.M., and Acsady, L. (2016). Thalamic Inhibition: Diverse Sources, Diverse Scales. Trends Neurosci. *39*, 680–693. .

Hofbauer, A., and Holländer, H. (1986). Synaptic connections of cortical and retinal terminals in the superior colliculus of the rabbit: an electron microscopic double labelling study. Exp. Brain Res. *65*, 145–155. .

Hoogland, P.V., Welker, E., and Van der Loos, H. (1987). Organization of the projections from barrel cortex to thalamus in mice studied with Phaseolus vulgaris-leucoagglutinin and HRP. Exp. Brain Res. *68*, 73–87. .

Kirchgessner, M.A., Franklin, A.D., and Callaway, E.M. (2021). Distinct “driving” versus “modulatory” influences of different visual corticothalamic pathways. Curr. Biol. *31*, 5121-5137.e7. .

Kitanishi, T., Tashiro, M., Kitanishi, N., and Mizuseki, K. (2022). Intersectional, anterograde transsynaptic targeting of neurons receiving monosynaptic inputs from two upstream regions. Commun Biol *5*, 149. .

Kleinfeld, D., Ahissar, E., and Diamond, M.E. (2006). Active sensation: insights from the rodent vibrissa sensorimotor system. Curr. Opin. Neurobiol. *16*, 435–444. .

Li, Z., Wei, J.-X., Zhang, G.-W., Huang, J.J., Zingg, B., Wang, X., Tao, H.W., and Zhang, L.I. (2021). Corticostriatal control of defense behavior in mice induced by auditory looming cues. Nat. Commun. *12*, 1040. .

Liang, F., Xiong, X.R., Zingg, B., Ji, X.-Y., Zhang, L.I., and Tao, H.W. (2015). Sensory Cortical Control of a Visually Induced Arrest Behavior via Corticotectal Projections. Neuron *86*, 755–767. .

Liu, X., Huang, H., Snutch, T.P., Cao, P., Wang, L., and Wang, F. (2022). The Superior Colliculus: Cell Types, Connectivity, and Behavior. Neurosci. Bull. https://doi.org/10.1007/s12264-022-00858-1.

Lohse, M., Dahmen, J.C., Bajo, V.M., and King, A.J. (2021). Subcortical circuits mediate communication between primary sensory cortical areas in mice. Nat. Commun. *12*, 3916. .

Madisen, L., Zwingman, T.A., Sunkin, S.M., Oh, S.W., Zariwala, H.A., Gu, H., Ng, L.L., Palmiter, R.D., Hawrylycz, M.J., Jones, A.R., et al. (2010). A robust and high-throughput Cre

reporting and characterization system for the whole mouse brain. Nat. Neurosci. *13*, 133–140. .

Mao, T., Kusefoglu, D., Hooks, B.M., Huber, D., Petreanu, L., and Svoboda, K. (2011). Long-range neuronal circuits underlying the interaction between sensory and motor cortex. Neuron *72*, 111–123. .

Mease, R.A., Sumser, A., Sakmann, B., and Groh, A. (2016). Corticothalamic Spike Transfer via the L5B-POm Pathway in vivo. Cereb. Cortex *26*, 3461–3475. .

Melzer, S., Michael, M., Caputi, A., Eliava, M., Fuchs, E.C., Whittington, M.A., and Monyer, H. (2012). Long-range-projecting GABAergic neurons modulate inhibition in hippocampus and entorhinal cortex. Science *335*, 1506–1510. .

Meredith, M.A., and Stein, B.E. (1986). Visual, auditory, and somatosensory convergence on cells in superior colliculus results in multisensory integration. J. Neurophysiol. *56*, 640–662. .

Mitchinson, B., Martin, C.J., Grant, R.A., and Prescott, T.J. (2007). Feedback control in active sensing: rat exploratory whisking is modulated by environmental contact. Proc. Biol. Sci. *274*, 1035–1041. .

Mukherjee, A., Bajwa, N., Lam, N.H., Porrero, C., Clasca, F., and Halassa, M.M. (2020). Variation of connectivity across exemplar sensory and associative thalamocortical loops in the mouse. Elife *9*. https://doi.org/10.7554/eLife.62554.

Muthuramalingam, M., and Bruecker, C. (2019). Seal and Sea lion Whiskers Detect Slips of Vortices Similar as Rats Sense Textures. Sci. Rep. *9*, 12808. .

Nyffeler, T., Kaufmann, B.C., and Cazzoli, D. (2021). Visual Neglect After an Isolated Lesion of the Superior Colliculus. JAMA Neurol. *78*, 1531–1533. .

Paxinos, G. (2001). The mouse brain in stereotaxic coordinates / George Paxinos, Keith B.J. Franklin (San Diego, Calif. ; London : Academic).

Petersen, C.C.H. (2019). Sensorimotor processing in the rodent barrel cortex. Nat. Rev. Neurosci. https://doi.org/10.1038/s41583-019-0200-y.

Petty, G.H., Kinnischtzke, A.K., Hong, Y.K., and Bruno, R.M. (2021). Effects of arousal and movement on secondary somatosensory and visual thalamus. Elife *10*. https://doi.org/10.7554/eLife.67611.

Prasad, J.A., Carroll, B.J., and Sherman, S.M. (2020). Layer 5 Corticofugal Projections from Diverse Cortical Areas: Variations on a Pattern of Thalamic and Extrathalamic Targets. J. Neurosci. *40*, 5785–5796. .

Robinson, D.L., and McClurkin, J.W. (1989). The visual superior colliculus and pulvinar. Rev. Oculomot. Res. *3*, 337–360. .

Rojas-Piloni, G., Guest, M., Johnson, A., Egger, R., Narayanan, R., Udvary, D., Sakmann, B., and Oberlaender, M. (2014). Cell type-specific subcortical targets of layer 5 projecting neurons in the rat vibrissal cortex.

Rojas-Piloni, G., Guest, J.M., Egger, R., Johnson, A.S., Sakmann, B., and Oberlaender, M. (2017). Relationships between structure, in vivo function and long-range axonal target of cortical pyramidal tract neurons. Nat. Commun. *8*, 870. .

Shang, C., Liu, A., Li, D., Xie, Z., Chen, Z., Huang, M., Li, Y., Wang, Y., Shen, W.L., and

Cao, P. (2019). A subcortical excitatory circuit for sensory-triggered predatory hunting in mice. Nat. Neurosci. *22*, 909–920. .

Sreenivasan, V., Esmaeili, V., Kiritani, T., Galan, K., Crochet, S., and Petersen, C.C.H. (2016). Movement Initiation Signals in Mouse Whisker Motor Cortex. Neuron *92*, 1368–1382. .

Steinmetz, N.A., Aydin, C., Lebedeva, A., Okun, M., Pachitariu, M., Bauza, M., Beau, M., Bhagat, J., Böhm, C., Broux, M., et al. Neuropixels 2.0: A miniaturized high-density probe for stable, long-term brain recordings. https://doi.org/10.1101/2020.10.27.358291.

Sumser, A., Mease, R.A., Sakmann, B., and Groh, A. (2017). Organization and somatotopy of corticothalamic projections from L5B in mouse barrel cortex. Proc. Natl. Acad. Sci. U. S. A. *114*, 8853–8858. .

Tamamaki, N., Yanagawa, Y., Tomioka, R., Miyazaki, J.-I., Obata, K., and Kaneko, T. (2003). Green fluorescent protein expression and colocalization with calretinin, parvalbumin, and somatostatin in the GAD67-GFP knock-in mouse. J. Comp. Neurol. *467*, 60–79. .

Wallace, M.T., Meredith, M.A., and Stein, B.E. (1993). Converging influences from visual, auditory, and somatosensory cortices onto output neurons of the superior colliculus. J. Neurophysiol. *69*, 1797–1809. .

White, E.L., Weinfeld, E., and Lev, D.L. (2004). Quantitative analysis of synaptic distribution along thalamocortical axons in adult mouse barrels. J. Comp. Neurol. *479*, 56–69. .

Whyland, K.L., Slusarczyk, A.S., and Bickford, M.E. (2020). GABAergic cell types in the superficial layers of the mouse superior colliculus. J. Comp. Neurol. *528*, 308–320. .

Xiong, X.R., Liang, F., Zingg, B., Ji, X.-Y., Ibrahim, L.A., Tao, H.W., and Zhang, L.I. (2015). Auditory cortex controls sound-driven innate defense behaviour through corticofugal projections to inferior colliculus. Nat. Commun. *6*, 7224. .

Zingg, B., Chou, X.L., Zhang, Z.G., Mesik, L., Liang, F., Tao, H.W., and Zhang, L.I. (2017). AAV-Mediated Anterograde Transsynaptic Tagging: Mapping Corticocollicular Input-Defined Neural Pathways for Defense Behaviors. Neuron *93*, 33–47. .

Zingg, B., Peng, B., Huang, J., Tao, H.W., and Zhang, L.I. (2020). Synaptic Specificity and Application of Anterograde Transsynaptic AAV for Probing Neural Circuitry. J. Neurosci. *40*, 3250–3267. .

Arenkiel, B.R., Peca, J., Davison, I.G., Feliciano, C., Deisseroth, K., Augustine, G.J., Ehlers, M.D., and Feng, G. (2007). In vivo light-induced activation of neural circuitry in transgenic mice expressing channelrhodopsin-2. Neuron 54, 205–218. .

Baek, J., Lee, S., Cho, T., Kim, S.-W., Kim, M., Yoon, Y., Kim, K.K., Byun, J., Kim, S.J., Jeong, J., et al. (2019). Neural circuits underlying a psychotherapeutic regimen for fear disorders. Nature 566, 339–343. .

Basso, M.A., and May, P.J. (2017). Circuits for Action and Cognition: A View from the Superior Colliculus. Annu Rev Vis Sci 3, 197–226. .

Basso, M.A., Bickford, M.E., and Cang, J. (2021). Unraveling circuits of visual perception and cognition through the superior colliculus. Neuron 109, 918–937. .

Benavidez, N.L., Bienkowski, M.S., Zhu, M., Garcia, L.H., Fayzullina, M., Gao, L., Bowman, I., Gou, L., Khanjani, N., Cotter, K.R., et al. (2021). Organization of the inputs and outputs of the mouse superior colliculus. Nat. Commun. 12, 1–20. .

Bezdudnaya, T., and Castro-Alamancos, M.A. (2011). Superior colliculus cells sensitive to active touch and texture during whisking. J. Neurophysiol. 106, 332–346. .

Bogadhi, A.R., Bollimunta, A., Leopold, D.A., and Krauzlis, R.J. (2019). Spatial Attention Deficits Are Causally Linked to an Area in Macaque Temporal Cortex. Curr. Biol. 29, 726–736.e4. .

Brecht, M., Naumann, R., Anjum, F., Wolfe, J., Munz, M., Mende, C., and Roth-Alpermann, C. (2011). The neurobiology of Etruscan shrew active touch. Philos. Trans. R. Soc. Lond. B Biol. Sci. 366, 3026–3036. .

Castro-Alamancos, M.A., and Favero, M. (2016). Whisker-related afferents in superior colliculus. J. Neurophysiol. 115, 2265–2279. .

Catania, K.C., Hare, J.F., and Campbell, K.L. (2008). Water shrews detect movement, shape, and smell to find prey underwater. Proc. Natl. Acad. Sci. U. S. A. 105, 571–576. .

Cavanaugh, J., Berman, R.A., Joiner, W.M., and Wurtz, R.H. (2016). Saccadic Corollary Discharge Underlies Stable Visual Perception. J. Neurosci. 36, 31–42. .

Chou, X.-L., Wang, X., Zhang, Z.-G., Shen, L., Zingg, B., Huang, J., Zhong, W., Mesik, L., Zhang, L.I., and Tao, H.W. (2018). Inhibitory gain modulation of defense behaviors by zona incerta. Nat. Commun. 9, 1151. .

Corneil, B.D., and Munoz, D.P. (2014). Overt responses during covert orienting. Neuron 82, 1230–1243. .

Duan, C.A., Pan, Y., Ma, G., Zhou, T., Zhang, S., and Xu, N.-L. (2021). A cortico-collicular pathway for motor planning in a memory-dependent perceptual decision task. Nat. Commun. 12, 2727. .

Feig, S., and Harting, J.K. (1992). Ultrastructural studies of the primate parabigeminal nucleus: electron microscopic autoradiographic analysis of the tectoparabigeminal projection in Galago crassicaudatus. Brain Res. 595, 334–338. .

Fenno, L.E., Mattis, J., Ramakrishnan, C., Hyun, M., Lee, S.Y., He, M., Tucciarone, J., Selimbeyoglu, A., Berndt, A., Grosenick, L., et al. (2014). Targeting cells with single vectors using multiple-feature Boolean logic. Nat. Methods 11, 763–772. .

Ford, J.M., and Mathalon, D.H. (2019). Efference Copy, Corollary Discharge, Predictive Coding, and Psychosis. Biol Psychiatry Cogn Neurosci Neuroimaging 4, 764–767. .

Gharaei, S., Arabzadeh, E., and Solomon, S.G. (2018). Integration of visual and whisker signals in rat superior colliculus. Sci. Rep. 8, 16445. .

Gong, S., Doughty, M., Harbaugh, C.R., Cummins, A., Hatten, M.E., Heintz, N., and Gerfen, C.R. (2007). Targeting Cre recombinase to specific neuron populations with bacterial artificial chromosome constructs. J. Neurosci. 27, 9817–9823. .

Groh, A., de Kock, C.P.J., Wimmer, V.C., Sakmann, B., and Kuner, T. (2008). Driver or coincidence detector: modal switch of a corticothalamic giant synapse controlled by spontaneous activity and short-term depression. J. Neurosci. 28, 9652–9663. .

Halassa, M.M., and Acsady, L. (2016). Thalamic Inhibition: Diverse Sources, Diverse Scales. Trends Neurosci. 39, 680–693. .

Hofbauer, A., and Holländer, H. (1986). Synaptic connections of cortical and retinal terminals in the superior colliculus of the rabbit: an electron microscopic double labelling study. Exp. Brain Res. 65, 145–155. .

Hoogland, P.V., Welker, E., and Van der Loos, H. (1987). Organization of the projections from barrel cortex to thalamus in mice studied with Phaseolus vulgaris-leucoagglutinin and HRP. Exp. Brain Res. 68, 73–87. .

Kirchgessner, M.A., Franklin, A.D., and Callaway, E.M. (2021). Distinct “driving” versus “modulatory”

influences of different visual corticothalamic pathways. Curr. Biol. 31, 5121–5137.e7. .

Kitanishi, T., Tashiro, M., Kitanishi, N., and Mizuseki, K. (2022). Intersectional, anterograde transsynaptic targeting of neurons receiving monosynaptic inputs from two upstream regions. Commun Biol 5, 149. .

Kleinfeld, D., Ahissar, E., and Diamond, M.E. (2006). Active sensation: insights from the rodent vibrissa sensorimotor system. Curr. Opin. Neurobiol. 16, 435–444. .

Li, Z., Wei, J.-X., Zhang, G.-W., Huang, J.J., Zingg, B., Wang, X., Tao, H.W., and Zhang, L.I. (2021). Corticostriatal control of defense behavior in mice induced by auditory looming cues. Nat. Commun. 12, 1040. .

Liang, F., Xiong, X.R., Zingg, B., Ji, X.-Y., Zhang, L.I., and Tao, H.W. (2015). Sensory Cortical Control of a Visually Induced Arrest Behavior via Corticotectal Projections. Neuron 86, 755–767. .

Liu, X., Huang, H., Snutch, T.P., Cao, P., Wang, L., and Wang, F. (2022). The Superior Colliculus: Cell Types, Connectivity, and Behavior. Neurosci. Bull. https://doi.org/10.1007/s12264-022-00858-1.

Lohse, M., Dahmen, J.C., Bajo, V.M., and King, A.J. (2021). Subcortical circuits mediate communication between primary sensory cortical areas in mice. Nat. Commun. 12, 3916. .

Madisen, L., Zwingman, T.A., Sunkin, S.M., Oh, S.W., Zariwala, H.A., Gu, H., Ng, L.L., Palmiter, R.D., Hawrylycz, M.J., Jones, A.R., et al. (2010). A robust and high-throughput Cre reporting and characterization system for the whole mouse brain. Nat. Neurosci. 13, 133–140. .

Mao, T., Kusefoglu, D., Hooks, B.M., Huber, D., Petreanu, L., and Svoboda, K. (2011). Long-range neuronal circuits underlying the interaction between sensory and motor cortex. Neuron 72, 111–123. .

Mease, R.A., Sumser, A., Sakmann, B., and Groh, A. (2016). Corticothalamic Spike Transfer via the L5B-POm Pathway in vivo. Cereb. Cortex 26, 3461–3475. .

Melzer, S., Michael, M., Caputi, A., Eliava, M., Fuchs, E.C., Whittington, M.A., and Monyer, H. (2012). Long-range-projecting GABAergic neurons modulate inhibition in hippocampus and entorhinal cortex. Science 335, 1506–1510. .

Meredith, M.A., and Stein, B.E. (1986). Visual, auditory, and somatosensory convergence on cells in superior colliculus results in multisensory integration. J. Neurophysiol. 56, 640–662. .

Mitchinson, B., Martin, C.J., Grant, R.A., and Prescott, T.J. (2007). Feedback control in active sensing: rat exploratory whisking is modulated by environmental contact. Proc. Biol. Sci. 274, 1035–1041. .

Mukherjee, A., Bajwa, N., Lam, N.H., Porrero, C., Clasca, F., and Halassa, M.M. (2020). Variation of connectivity across exemplar sensory and associative thalamocortical loops in the mouse. Elife 9. https://doi.org/10.7554/eLife.62554.

Muthuramalingam, M., and Bruecker, C. (2019). Seal and Sea lion Whiskers Detect Slips of Vortices Similar as Rats Sense Textures. Sci. Rep. 9, 12808. .

Nyffeler, T., Kaufmann, B.C., and Cazzoli, D. (2021). Visual Neglect After an Isolated Lesion of the Superior Colliculus. JAMA Neurol. 78, 1531–1533. .

Paxinos, G. (2001). The mouse brain in stereotaxic coordinates / George Paxinos, Keith B.J. Franklin (San Diego, Calif. ; London : Academic).

Petersen, C.C.H. (2019). Sensorimotor processing in the rodent barrel cortex. Nat. Rev. Neurosci. https://doi.org/10.1038/s41583-019-0200-y.

Petty, G.H., Kinnischtzke, A.K., Hong, Y.K., and Bruno, R.M. (2021). Effects of arousal and movement on secondary somatosensory and visual thalamus. Elife 10. https://doi.org/10.7554/eLife.67611.

Prasad, J.A., Carroll, B.J., and Sherman, S.M. (2020). Layer 5 Corticofugal Projections from Diverse

Cortical Areas: Variations on a Pattern of Thalamic and Extrathalamic Targets. J. Neurosci. 40, 5785–5796. .

Robinson, D.L., and McClurkin, J.W. (1989). The visual superior colliculus and pulvinar. Rev. Oculomot. Res. 3, 337–360. .

Rojas-Piloni, G., Guest, M., Johnson, A., Egger, R., Narayanan, R., Udvary, D., Sakmann, B., and Oberlaender, M. (2014). Cell type-specific subcortical targets of layer 5 projecting neurons in the rat vibrissal cortex.

Rojas-Piloni, G., Guest, J.M., Egger, R., Johnson, A.S., Sakmann, B., and Oberlaender, M. (2017). Relationships between structure, in vivo function and long-range axonal target of cortical pyramidal tract neurons. Nat. Commun. 8, 870. .

Shang, C., Liu, A., Li, D., Xie, Z., Chen, Z., Huang, M., Li, Y., Wang, Y., Shen, W.L., and Cao, P. (2019). A subcortical excitatory circuit for sensory-triggered predatory hunting in mice. Nat. Neurosci. 22, 909–920. .

Sreenivasan, V., Esmaeili, V., Kiritani, T., Galan, K., Crochet, S., and Petersen, C.C.H. (2016). Movement Initiation Signals in Mouse Whisker Motor Cortex. Neuron 92, 1368–1382. .

Steinmetz, N.A., Aydin, C., Lebedeva, A., Okun, M., Pachitariu, M., Bauza, M., Beau, M., Bhagat, J., Böhm, C., Broux, M., et al. Neuropixels 2.0: A miniaturized high-density probe for stable, long-term brain recordings. https://doi.org/10.1101/2020.10.27.358291.

Sumser, A., Mease, R.A., Sakmann, B., and Groh, A. (2017). Organization and somatotopy of corticothalamic projections from L5B in mouse barrel cortex. Proc. Natl. Acad. Sci. U. S. A. 114, 8853–8858. .

Wallace, M.T., Meredith, M.A., and Stein, B.E. (1993). Converging influences from visual, auditory, and somatosensory cortices onto output neurons of the superior colliculus. J. Neurophysiol. 69, 1797–1809. .

White, E.L., Weinfeld, E., and Lev, D.L. (2004). Quantitative analysis of synaptic distribution along thalamocortical axons in adult mouse barrels. J. Comp. Neurol. 479, 56–69. .

Whyland, K.L., Slusarczyk, A.S., and Bickford, M.E. (2020). GABAergic cell types in the superficial layers of the mouse superior colliculus. J. Comp. Neurol. 528, 308–320. .

Xiong, X.R., Liang, F., Zingg, B., Ji, X.-Y., Ibrahim, L.A., Tao, H.W., and Zhang, L.I. (2015). Auditory cortex controls sound-driven innate defense behaviour through corticofugal projections to inferior colliculus. Nat. Commun. 6, 7224. .

Zingg, B., Chou, X.L., Zhang, Z.G., Mesik, L., Liang, F., Tao, H.W., and Zhang, L.I. (2017). AAV-Mediated Anterograde Transsynaptic Tagging: Mapping Corticocollicular Input-Defined Neural Pathways for Defense Behaviors. Neuron 93, 33–47. .

Zingg, B., Peng, B., Huang, J., Tao, H.W., and Zhang, L.I. (2020). Synaptic Specificity and Application of Anterograde Transsynaptic AAV for Probing Neural Circuitry. J. Neurosci. 40, 3250–3267. .

# STAR★Methods

## Key Resources Table

| Reagent or Resource | Source | Identifier |
|---|---|---|
| Antibodies | | |
| primary antibody rabbit IgG anti-NeuN | Merck Chemicals GmbH | ABN78 |
| primary antibody rabbit IgG anti-GABA | Sigma-Aldrich | A2052 |
| secondary antibody goat anti-rabbit IgG (H+L) Alexa 647 | Thermo Fisher Scientific/ Invitrogen | A32733 |
| Bacterial and virus strain | | |
| PENN AAV hSyn Cre WPRE hGH | Addgene | #105553-AAV1 |
| AAV2-hSyn-DIO-EGFP | Addgene | #50457-AAV2 |
| AAV2hSyn-DIO-mCherry | Addgene | #50459-AAV2 |
| AAV8-hSyn Con/Fon EYFP | Addgene | #55650-AAV8 |
| AAV2-Ef1a-fDIO mCherry | Addgene | #114471-AAV2 |
| AAV1-EF1a-Flpo | Addgene | #55637-AAV1 |
| AAVrg-CAG-hChR2-tdTomato | Addgene | #28017-AAVrg |
| AAV1/2-CAG-SyPhy-EGFP | Thomas Kuner Lab | N/A |
| AAV1/2-CBA-SyPhy-mOrange | Thomas Kuner Lab | N/A |
| Experimental models: organisms/strains | | |
| (B6.FVB(Cg)-Tg/(Ntsr1-Cre)GN220Sat/Mmucd<br>x<br>B6.129S-Gt(ROSA)26Sortm32(CAG-COP4*H134R/EYFP). | GENSAT Project at Rockefeller University<br><br>Jackson Laboratory<br>Created by: Hongkui Zeng | MGI:4358487<br>(MMRRC: 030648)<br><br>MGI:5013789 |
| “Wild type”; C57BL/6N | Janvier | C57BL/6NRj Mouse - Janvier Labs (janvier-labs.com) |

| | | |
|---|---|---|
| B6-Gad1tm2(Cre)Mony/Uhg | Hannah Monyer | MGI:4830465 |
| B6.CG-Gad1TM1Tama | Created by: Nobuaki Tamamaki | (Tamamaki et al., 2003) |
| (B6.FVB/CD1-Tg(Rbp4-Cre)KL100Gsat/Mmucd<br>x<br>B6.129S-Gt(ROSA)26Sortm32(CAG-COP4*H134R/EYFP) | GENSAT Project at Rockefeller University<br>Jackson Laboratory<br>Created by: Hongkui Zeng | MGI:4367067 (MMRRC:031125)<br>MGI:5313002 |
| Software and algorithms | | |
| Matlab 2018b | Mathworks | https://de.mathworks.com/products/matlab.html |
| Spike 2 | CED | https://ced.co.uk/es/products/spkovin |
| ImageJ/Fiji | NIH | https://imagej.net/software/fiji/downloads |
| Canvas X | ACD systems | |
| Microsoft office | Microsoft | www.microsoft.com |
| Kilosort 2.0 | Github | https://github.com/MouseLand/Kilosort |
| Phy | The Cortical Processing Laboratory at UCL | https://github.com/cortex-lab/phy.git |

**Materials availability**

This study did not generate new unique reagents or mouse lines

**Resource availability**

All data and analysis scripts of this paper will be shared by the lead contact upon reasonable request.

**Lead contact**

Further information and requests for data or code should be directed to and will be fulfilled by the lead contact, Jesus Martin-Cortecero or Alexander Groh.

**Materials availability**

This study did not generate new unique reagents or mouse lines

**Animals**

Mice (male and female, 10-20 weeks of age at the time of virus injection) were housed with food and water ad libitum on a 12h light/dark cycle. All experimental procedures were performed according to the ethical guidelines set by the governing body (Regierungspräsidium Karlsruhe, Germany).

Mouse lines

Retrograde labeling:

“Ntsr1-EYFP”; crossbreed between “Ntsr1-Cre” x “Ai32” (B6.FVB(Cg)-Tg/(Ntsr1-Cre)GN220Sat/Mmucd x B6.129S-Gt(ROSA)26Sortm32(CAG-COP4*H134R/EYFP).

RN labeling: “Wild type”; C57BL/6N

iRN labeling: “GAD-Cre”; B6-Gad1tm2(Cre)Mony/Uhg

Quantification of GABAergic neurons in intermediate layers of SC:

“GAD67-GFP”; B6.CG-Gad1TM1Tama

In vivo Electrophysiology:

“Rbp4-Cre-ChR2-EYFP”; crossbreed between “Rbp4-Cre” x “Ai32” (B6.FVB/CD1-Tg(Rbp4-Cre)KL100Gsat/Mmucd x B6.129S-Gt(ROSA)26Sortm32(CAG-COP4*H134R/EYFP)

**Virus-mediated labeling and intersectional strategies**

*Retrograde labeling*: to identify whisker-related SC projection sites (Fig. 1A) we injected the retrograde rAAV-TdTomato (Mao et al., 2011) into LSC. To delineate cortical SC projection neurons (Td-Tomato) from layer 6 neurons, these injections were done in Ntsr1-EYFP mice, in which layer 6 (L6) but not L5 neurons express EYFP (Gong et al., 2007; Madisen et al., 2010).

*Cortico-collicular bouton labeling:* to label MC and BC boutons in SC we injected AAV1/2-CAG-SyPhy-EGFP and AAV1/2-CBA-SyPhy-mOrange (Sumser et al., 2017) into the cortical projection sites (BC and MC, respectively) in the same animal. The diameters of synaptic boutons labeled with Synaptophysin-EGFP and Synaptophysin-mOrangein SC were measured as maximal projection area (Mukherjee et al., 2020; Prasad et al., 2020) from confocal microscopy images using an A1+ microscope and NIS elements (Heidelberg Nikon Imaging Center).

*Transsynaptic anterograde labeling:* to label input-specific recipient neurons we made use of the ability of AAV1-Cre and AAV1-Flpo particles to jump to postsynaptic neurons via vesicle release (Fenno et al., 2014; Zingg et al., 2017, 2020). We adopted this strategy to reveal different subsets of SC neurons defined by their monosynaptic input from whisker-related projection sites of interest (MC, BC, Bs): 1. *Recipient neurons (RNs)*, 2. *Cortical and brainstem RNs,* 3. *Recipient inhibitory neurons (iRNs)* and 4. *Convergence neurons (CVG-RNs)* as follows:

*1. Recipient neurons (RNs)*: cocktails of AAV1-Cre + AAV2-DIO-mCherry (1:1) were injected into the projection sites of interest (MC, BC, Bs) in separate mice. A second injection of the Cre reporter virus AAV2-DIO-EGFP was targeted to SC to reveal RNs (Fig. 2A).

*2. Cortical and brainstem RNs:* Same as RN but injecting MC and BC in the same mouse with a cocktail of AAV1-Flpo + AAV2-fDIO-mCherry (1:1), and Bs with a cocktail of AAV1-Cre + AAV2-DIO-EGFP (1:1). SC was injected with a cocktail of AAV2-fDIO-mCherry + AAV2-DIO-EGFP (1:1) to reveal cortical and brainstem RNs in different colors.

*3. Inhibitory recipient neurons (iRNs)*: same as RN approach but in GAD-Cre mice (Melzer et al., 2012)(Fig. 3A), using a cocktail of AAV1-Flpo + AAV2-fDIO-mCherry (1:1) for the projection sites of interest (MC, BC, Bs). SC was targeted with a cocktail of AAV8-Con/Fon-EYFP and AAV2-fDIO-mCherry (1:1). AAV8-Con/Fon-EYFP serves as a reporter virus to express EGFP when Cre and Flpo recombinases are co-expressed and thus labels iRNs, while AAV2-fDIO-mCherry labels RNs.

*4. Convergence neurons (CVG-RNs)*: AAV1-Flpo + AAV2-fDIO-mCherry (projection site 1) and AAV1-Cre + AAV2-DIO-mCherry (projection site 2) cocktails (1:1) were injected into wild-type mice, and an AAV8-Con/Fon-EYFP + AAV2-fDIO-mCherry cocktail (1:1) into SC to visualize convergent RNs (EYFP, co-innervated from projection sites 1 + 2, Fig. 4A) and RNs (mCherry, innervated from projection site 1 only). See supplementary Fig. S6 for controls of the conditional expression systems. Virus expression time was between 28-30 days.

| Virus | Virus short name | Titer in viral genomes per milliliter [vg/ml] | Supplier | Expression |
|---|---|---|---|---|
| PENN AAV hSyn Cre WPRE hGH | AAV-1-Cre | $1.8 \times 10^{13}$ | Addgene #105553-AAV1 | Cre |
| AAV2-hSyn-DIO-EGFP | DIO-EGFP | $3 \times 10^{12}$ | Addgene #50457-AAV2 | Cre dependent EGFP |
| AAV2hSyn-DIO-mCherry | DIO mCherry | $4 \times 10^{12}$ | Addgene #50459-AAV2 | Cre dependent mCHerry |
| AAV8-hSyn Con/Fon EYFP | Con/Fon EYFP | $1 \times 10^{13}$ | Addgene #55650-AAAV8 | Cre and Flpo dependent EYFP |
| AAV2-Ef1a-fDIO mCherry | fDIO mCherry | $1.1 \times 10^{13}$ | Addgene #114471-AAV2 | Flpo dependent mCherry |
| AAV1-EF1a-Flpo | AAV1-Flpo | $7 \times 10^{12}$ | Addgene #55637-AAV1 | Flpo |
| AAV1-Ef1a-fDIO EYFP | fDIO EYFP | $2.1 \times 10^{13}$ | Addgene #55641-AAV1 | Flpo dependent |
| AAVrg-CAG-hChR2-tdTomato (AAV Retrograde) | rAAV-TdTomato | $7 \times 10^{12}$ | Addgene #28017-AAVrg | tdTomato |
| AAV1/2-CAG-SyPhy-EGFP | AAV-SyPhy | Not determined | T.Kuner Lab | EGFP |
| AAV1/2-CBA-SyPhy-mOrange | AAV-SyPhy | Not determined | T.Kuner Lab | mOrange |

**Table 1. Viruses used for the different targeting strategies in this study.**

### Stereotaxic surgeries

Mice were placed in a stereotaxic frame (Kopf Instruments) and anesthetized with 1.2-2 vol%
5 isoflurane in medical oxygen at a flow rate of 0.8 l/min while keeping body temperature at 39°C. Carprofen (CP-Pharma) was administered subcutaneously (5 mg/kg) and lidocaine (Xylocaine 1%, Aspen Pharma) was injected under the scalp and around ear bars for local anesthesia. Eyes were covered with Bepanthen ointment (Bayer) to keep them lubricated

during the surgery. After ensuring the absence of tail- and toe-pinch reflexes, the skin was opened with a midline incision, the periosteum and aponeurotic galea were removed to visualize the reference points bregma and lambda, and the head was aligned to the stereotaxic frame. Small craniotomies were drilled above the injection sites and viral particle solutions were injected with calibrated glass micropipettes (Blaubrand; IntraMARK) at the following coordinates relative to bregma (AP, ML) and pia (DV):

| | **Injection volume [nl]** | **AP [mm]** | **ML [mm]** | **DV [mm]** |
|---|---|---|---|---|
| MC | 200 | 1 | 1 | -0.6 to -0.8 |
| BC | 200 | -1 | 2.95 | -0.6 to -0.8 |
| Bs (Sp5o) | 200 | -5.9 | 1.7 | -4 to -4.2 |
| SC | 300 | -3.6 | 1.3 | -2 / -1.8 / -1.6<br>(3 injections, 100 nl each) |

**Table 2. Coordinates and injection volumes for stereotaxic AAV injections.**

After viral particle injections, the pipette was left in place for 10 minutes to allow diffusion, and was then slowly retracted. Finally, the skin above the skull was sutured with silk (PermaHand, 6–0; Ethicon) and the animal was transferred to its home cage.

**Slicing and immunolabeling**

After virus expression, mice were exposed to a lethal dose of Ketamine (80 mg/kg) and Xylazine (10 mg/kg) and transcardially perfused with 4% paraformaldehyde (PFA) in PBS. The brain was removed and postfixed for 12 h in 4% PFA at 4°C. The same procedure was applied for GABA immunofluorescence labeling except using 2% glutaraldehyde and 2% PFA in PBS. Brains were sliced (50 μm) with a vibratome (Thermo Scientific Microm HM650V).

<u>NeuN immunofluorescence staining:</u>

SC slices were incubated in blocking solution (PB 0.1 M, with 4% normal goat antiserum (NGS, Biozol) and 0.4% Triton X-100 (Roth)) for 2 h, then washed 5 times in PB 0.1 M. Subsequently, slices were treated with primary antibody rabbit IgG anti-NeuN (Merck, ABN78) diluted in PB 0.1 M 1:500 with 1% NGS for 48 h at 4ºC. Finally, after washing again 5 times with PB 0.1 M, slices were incubated for 2 h at room temperature in secondary antibody goat anti-rabbit IgG (H+L) Alexa 647 (Invitrogen, A32733) diluted 1:500 in PB 0.1 M containing 0.3% Triton X-100 and 3% NGS.

GABA immunofluorescence staining:

SC slices were preincubated in PB 0.1 M containing 1% sodium borohydride for 15 min to remove glutaraldehyde autofluorescence. Subsequently, SC slices were washed three times in PB 0.1 M and then incubated in a blocking solution (4% NGS and 0.3% Triton X-100 in PB 0.1 M) for 30 min. We then washed the slices 5 times in PB 0.1 M and incubated them with primary antibody rabbit IgG antiGABA (Sigma A2052) diluted in PB 0.1 M 1:1000 with 1% NGS overnight at 4ºC. The following day, we washed 5 times with PB 0.1 M and incubated them for 1 h at room temperature in secondary antibody goat anti-rabbit IgG (H+L) Alexa 647 (Invitrogen, A32733) diluted 1:1000 in PB 0.1 M containing 1% NGS. Finally, slices were washed 5 times in PB 0.1 M and mounted with a mounting solution (Mowiol 4-88, Sigma-Aldrich).

**Microscopy**

Injection sites, labeled cells in SC, and axonal outputs were imaged with a fluorescent microscope (Leica DM6000) outfitted with an automated stage to generate mosaics (Andor Neo camera, SCC02104) and laser lines 365, 470, 505, 530, and 625 nm. The objective HC PL APO 10x/0.40Dry was used to image the injection site and labeled cells in SC (voxel size 2 x 2 µm). We used the objective HC PL APO 20x/0.70Dry (voxel size 1 x 1 µm) for imaging RN axonal outputs. Varicosities, retrogradely labeled cells, and immunolabeled cells were imaged with a confocal microscope (Nikon A1R or C2, Nikon Imaging Center Heidelberg, Germany) outfitted with an automated mosaic stage and laser lines 405, 488, 561, and 640 nm. Objectives used: Nikon Plan Apo 20x NA 0.75 Nikon Plan Fluor 40x NA 1.30 oil immersion, Nikon Apo λS 60x NA 1.40. Slices were scanned in sequential mode; scanner zoom: 1x to 3x; resolution of individual tiles: 2048 × 2048 pixels. The laser power, photomultiplier gain, and pinhole (20 - 60 µm) were adjusted so that the signal was not saturated.

**Cell counting**

Fluorescence image series of SC were loaded into Fiji and manually rotated to align all slices along the midline. From each image series, we selected the section that matched the most rostral part of SC (AP: -3.08 mm) in Paxinos' atlas (Paxinos, 2001), so that all series contained the same domain (AP: -3.08 to -4.28 mm). To select the most rostral section, we compared the shape and size of the hippocampus, optic tract, anterior pretectal nucleus, medial geniculate nucleus, and SC and its brachium anatomical references against Paxinos' -3.08 mm slice. The resulting SC series were processed in Fiji as follows. First, as a measure of background, we took the average pixel intensity of three different regions in the non-recipient area and subtracted this average value from each section in the series. Images were then

contrast-enhanced with an exponential transformation (Fiji “Exp" function) and brightness was manually restored by scaling intensity values by a factor between 1.2 and 2. Labeled neurons were detected using Fiji 3D Object Counter with two user parameters: gray-value threshold and a minimum-size filter, which we set to 30 pixels to exclude non-somatic signals. The distributions of detected neurons across the anterior-posterior (AP) SC axis are shown in 13 bins of 100 μm from -3.08 to -4.28 mm.

To estimate the proportion of GABAergic neurons in the intermediate layer of LSC, confocal image series of double-immunolabeled slices (GAD67 & NeuN) were analyzed with Fiji’s “Cell Counter” plugin. GAD67 and NeuN labeled somata were counted in three segments of 200×200 μm per image within the intermediate layer (n = 10 slices). We excluded marginal slices when the cell number did not satisfy a minimum *N* sample criteria to detect the proportion difference with a statistical power of 0.8 β.

**RN distribution analysis**

All analyses were done using MATLAB (R2018b). For comparisons across different RNs, neuron counts were normalized to the maximum value across sections within the same brain. Normality of the distributions was tested with one-sample Kolmogorov-Smirnov test and differences between the distributions were tested with Wilcoxon rank sum test. Mean values were reported with SEM (error bars or plus/minus) and median values with Q1 and Q3, or interquartile range (IQR). To compare distributions among different RN groups, a non-parametric analysis of variance was performed (Kruskal-Wallis and multiple comparisons test, using the Bonferroni method).

**Axon maps**

Fluorescent axonal projections from SC-RNs were reconstructed in Canvas X (version 10, ACD system). Coronal images were desaturated, inverted, and manually registered to the corresponding atlas section (Paxinos, 2001), see schematics in Fig. 6A, B, Supplementary Fig. S8). We considered axonal signals in the AP regions between -1.22 and -2.54 mm (diencephalon) and -5.4 and -6.4 mm (brainstem). The resulting axon counts were organized into two matrices (for diencephalon and brainstem, respectively) per input-defined RNs. Each matrix was $m \times n$, where $m$ is the number of 100 μm-bins in the AP dimension and $n$ is the number of nuclei analyzed; 15 for diencephalon and 7 for brainstem (Table 3).

| RN output type | Diencephalic axon map | Brainstem axon map |
|---|---|---|
| MC-RN | 13 slices x 15 nuclei | 11 slices x 7 nuclei |
| BC-RN | 13 slices x 15 nuclei | 14 slices x 7 nuclei |
| Bs-RN | 12 slices x 15 nuclei | 13 slices x 7 nuclei |

**Table 3. Axon-count matrices.**

Relative axon counts (RAC, normalized counts) were calculated for each pathway across the AP axis based on their maximum count as follows:

$$RAC = \frac{\#counts}{max(\#counts)}$$

RAC maps were visualized using MATLAB's built-in function contour ("Fill", "on") and are shown in descending order taking MC-RNs as reference. Finally, to compare the projection patterns among different RN groups, we summed the axonal counts per nuclei across the antero-posterior (*m*) dimension and calculated the z-score of the total axonal count per nucleus (*n*) (Fig. 6C, D).

**In vivo electrophysiological recordings**

Preparation and silicon-probe recordings

Preparations and recordings were done in 8-12 week-old Rbp4-Cre-ChR2-EYFP mice (n = 4), which is crossbred between "Rbp4-Cre" x "Ai32" to specifically express ChR2 in L5 PT neurons (Kirchgessner et al., 2021). Mice were anesthetized with a mixture of 5% urethane solution (i.p., 1.3 g/kg body weight) and 1% isoflurane in medical degree oxygen, applied via an inhalator mask. After incision, bregma and lambda were revealed and aligned using a micro-manipulator (Luigs-and-Neumann) to drill craniotomies above SC (AP: -3.6, ML: 1.3), BC (AP: -1, ML: +3), and MC (AP: +1, ML: +1). SC activity was recorded using an electrophysiology system composed of a multielectrode silicon probe in AP: -3.6, ML: +1.3 DV: -1.6 to -2 mm (sharpened ASSY-77 E1, Cambridge Neurotech); a 64-channel amplifier chip (RHD2164) to a USB-2 interface board (RHD-EVAL, Intan Technologies, California, US); and the Spike2 (version 9.14) recording suite with Intan Talker module (Cambridge Electronic Devices, Cambridge, UK). Neural activity was recorded at 30 kHz using a 100 Hz - 10 kHz bandpass filter. The resulting file (.smrx) was converted into a binary file (.bin) to feed it to Kilosort, a MATLAB-based semi-automated spike-sorting software (Steinmetz et al.). The file conversion consisted of reading the channels in the .smrx file, transforming them into unsigned 16-bit integers (uint16) values from the 16-bit depth analog-to-digital converter (ADC), and writing them into a .bin file. The .bin files and the E1-probe channel map in µm were input to

Kilosort with the default parameters and the results were curated with Phy. Single units with <3% refractory period (1.5 ms) violations and a baseline spike rate >0.1 Hz were included for subsequent analysis.

Optogenetic stimulation

An optical fiber was placed at an angle of ~45º, at ~100 µm from the pia to optogenetically activate L5 neurons in MC or BC. Optogenetic stimulation pulses were controlled by a stimulation protocol prepared in Spike2 through interface hardware (Power1401, Cambridge Electronic Design, Cambridge, UK). Single 5 ms laser-pulses (20 – 50 mW/mm$^2$ at the fiber tip) were delivered every 5 s using a custom-build laser setup containing a 488 nm solid-state laser (Sapphire, Coherent, Germany, maximum power 22 mW); an ultrafast shutter (Uniblitz, Rochester, NY, USA); and a collimator to focus the laser beam into the optical fiber (inner diameter 400 µm, NA 0.48, Thorlabs, USA). After stimulating L5 in one cortex, the optical fiber was moved to the other,e.g. MC and then BC.

Whisker stimulation

Whiskers (rows A to C, and arcs 1 to 3) were stimulated with a custom-built grid stimulator. An insect net was attached to a piezo-electric actuator (PL140.11, Piezotechnology, Germany), which was controlled by a stimulation protocol prepared in Spike2 through an Power1401 interface. The piezo command signal was amplified from 5 to 60 V with the piezo amplifier module from the Modular Electronics for Cell Physiology (Max-Planck-Institute for Medical Research, manufactured by Sigmann Elektronik, GmbH, Germany). Whisker deflections lasted 50 ms and were applied in 3 s intervals (0.33 Hz).

Cell responsiveness

*Whisker responses*: We considered a single unit to be whisker responsive if the spike count median across trials within a 14 ms window (-20 to -6 ms) pre-stimulus was significatively different from the spike count median within an identical-length window (6 to 20 ms, α=5%, two-sample Wilcoxon test).

*Optogenetic responses*: We considered two equal-length time windows in which we counted spikes before the onset of the optogenetic stimulus (spontaneous, -18 to -6 ms) and after the optogenetic stimulus onset (evoked, 6 to 18 ms) for each trial and for each unit. We computed the z-scores of evoked counts using the mean and standard deviation of spontaneous counts and compared evoked z-scores against a 1.96 z-threshold (α=5%). Trials that crossed the z-threshold were considered significantly responsive and were assigned a logical true value. We then computed the proportion of responsive (successful) trials per unit. In order to state significance for the response proportion, we estimated the necessary trial number (N) to

achieve a statistical power of 0.8 with proportion values $p$ and hypothesis $p_0=1-p$ using MATLAB's test of the 'N' parameter (trials) for a binomial distribution (sampsizepwr). For $p\approx1/3$, $N\approx40$, which is our experimental trial number. Additionally, we compared the unit's trial crossing proportions with increasing thresholds (α=5%, one-tailed *t*-test, ttest in MATLAB) and visually searched for a region where the cardinality of included units stabilized. With an increasing threshold, the number of included units decreases until the responsive units would be found. We chose $p_0=1/3$ as an optimal inflection point, minimizing the threshold and maximizing the responsive unit cardinality.

**Supplementary information**

# Trans-collicular pathways for sensory-motor integration in the whisker system

Jesús Martín-Cortecero [a,1,*], Emilio Ulises Isaías-Camacho[a,1], Berin Boztepe[a,b,1], Katharina Ziegler [a], Rebecca Audrey Mease[a] and Alexander Groh [a,*]

[a] Medical Biophysics, Institute for Physiology and Pathophysiology, Heidelberg University, 69120, Germany.
[b] Current affiliation: Neuroradiology Department, University Hospital Heidelberg, 69120 Heidelberg, Germany
[1] JMC, EIC, and BB contributed equally to this work
[*] To whom correspondence may be addressed. Email: martin-cortecero@physiologie.uni-heidelberg.de; groh@uni-heidelberg.de

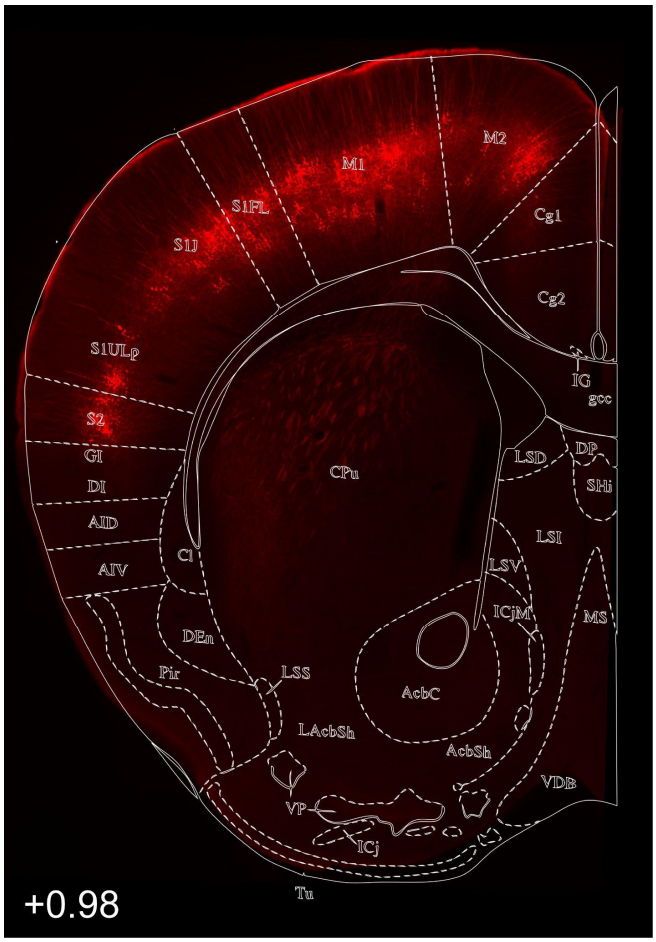


**Fig. S1. LSC-projecting neurons in the motor cortex (M1 and M2). Related to Fig.1**

Retrograde mCherry-labeled LSC-projecting neurons (red) in the motor cortex (MC) extend across M1 and M2.

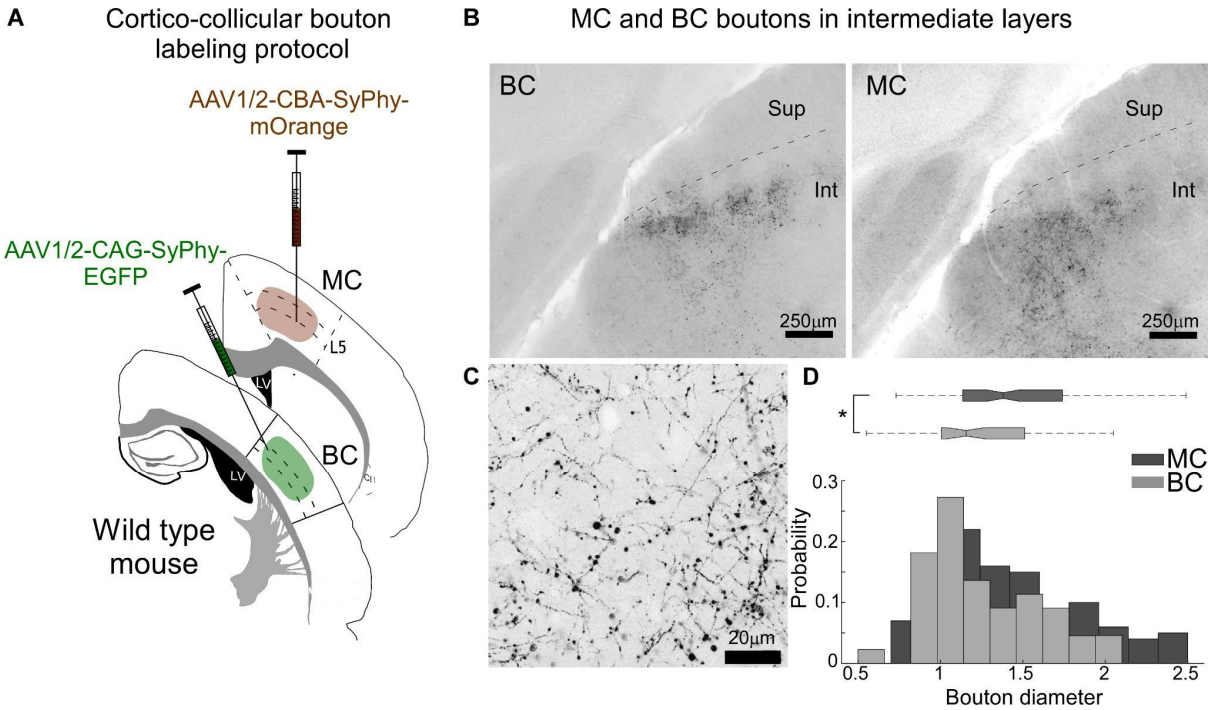


**Fig. S2. MC and BC boutons in SC. Related to Fig.1.**

*(A)* Schematic of dual injections of AAVs encoding for synapse-specific fluorescent fusion proteins (Synaptophysin-mOrange, Synaptophysin-EGFP (Groh et al., 2008; Sumser et al., 2017)) to label MC (mOrange) and BC (EYFP) boutons in SC.

*(B)* Example confocal images of coronal SC slices with fluorescently labeled BC (left, synaptophysin-EGFP) and MC (right, synaptophysin-mOrange) boutons. Sup: superficial layer, Int: intermediate layer.

*(C)* Example of higher magnification confocal image showing BC boutons in the intermediate layers of SC.

*(D)* Normalized distribution of MC and BC bouton diameters in SC. Boxplots of median bouton diameters (BC = 1.15 µm, n = 100; MC = 1.38 µm, n = 44) and IQRs (BC = 0.50 µm; MC = 0.60 µm). * represents $p < 0.01$; B:Wilcoxon rank sum; exact p values in Supplementary Table S1.

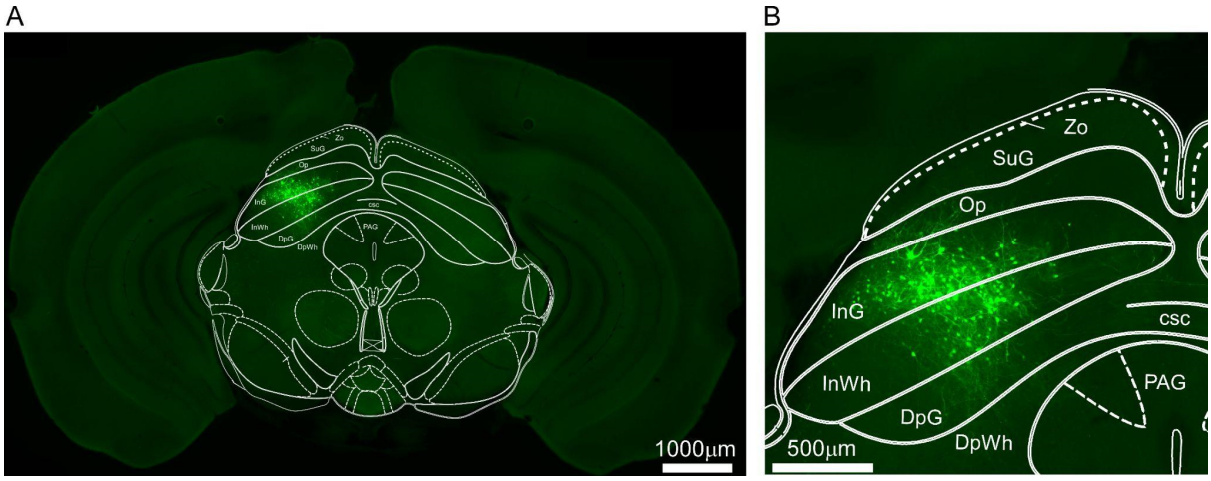


**Fig. S3. Transsynaptic labeling of MC recipient neurons in the intermediate gray and white layers** (Paxinos, 2001)**, equivalent to SC intermediate layers. Related to Fig. 2.**

*(A)* SC coronal slice showing transsynaptically EGFP-labeled MC-RNs in the intermediate layers of SC with overlaid anatomical borders from Paxinos mouse brain atlas (Paxinos, 2001).
*(B)* Same as (A) at higher magnification.
Abbreviations: csc, commissure of the superior colliculus; DpG, Deep gray layer; DpWh deep white layer; InG, Intermediate gray layer; InWh, intermediate white layer; Op, optic nerve of the superior colliculus; PAG, periaqueductal gray; SuG, superficial gray layer; Zo, Zonal layer.

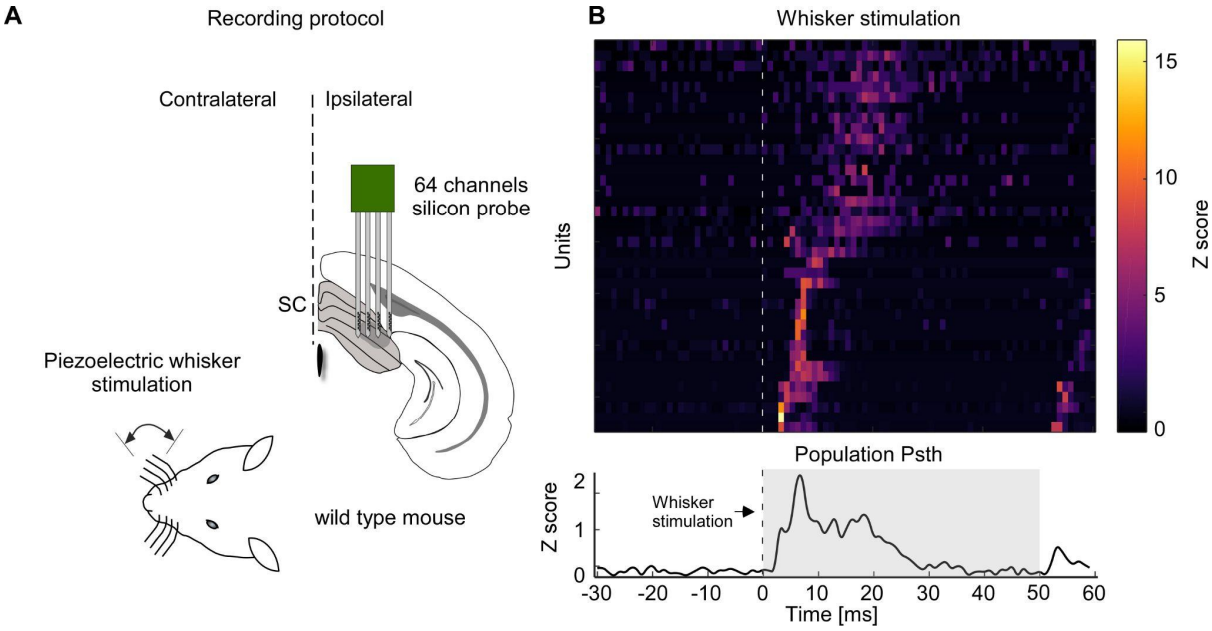


**Fig. S4. Whisker responses in the lateral SC. Related to Fig. 2.**

*(A)* Experimental schematic of whisker stimulation with a piezoelectric actuator and silicon probe recording in LSC in anesthetized mice.
*(B)* Top: single unit PSTHs in response to whisker stimulation (stippled line); units were ordered by first-spike latency, with shortest latencies on the bottom (38 units, 3 mice). Bottom: LSC population PSTHs in response to whisker stimulation (gray box, onset marked with stippled line).

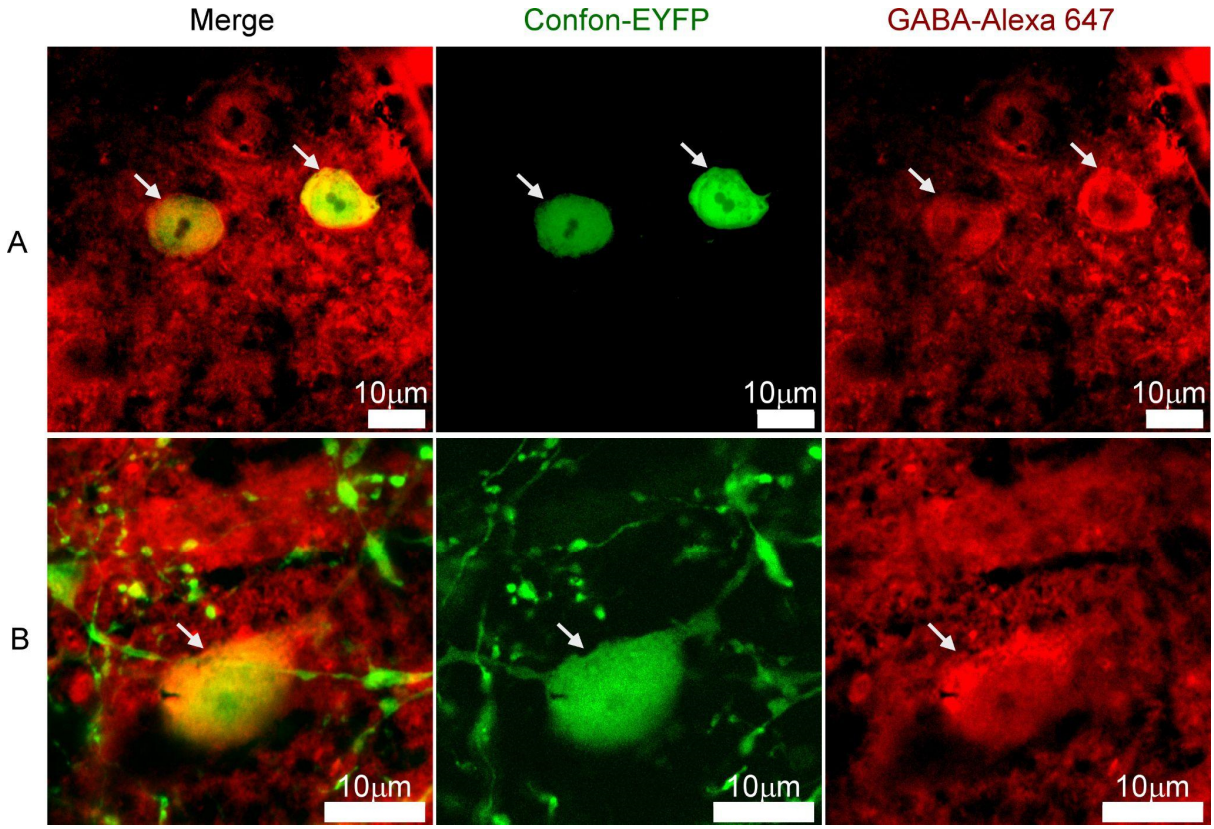


**Fig. S5. GABA immunostaining of Con/Fon labeled cells in the GAD-Cre mouse line. Related to Fig. 3.**

Example experiment in which MC-iRNs were labeled by injecting AAV1-Flpo in MC, and AAV8-Con/Fon-EYFP in LSC of GAD-Cre mice. Slices with transsynaptically labeled iRNs (green, Confon-EYFP) were counterstained against GABA (red, immunostaining with Alexa 647, see Methods). All inspected iRNs were GABA positive.

*(A)* Example confocal image showing iRNs (green) and GABA immunostain (red). Left: overlay of red and green channel, showing GABA positive iRNs in yellow (arrows). Middle: green channel, showing iRNs (green). Right: red channel, showing GABA positive somata (red).

*(B)* Same as in (A) for a different iRN at higher magnification.

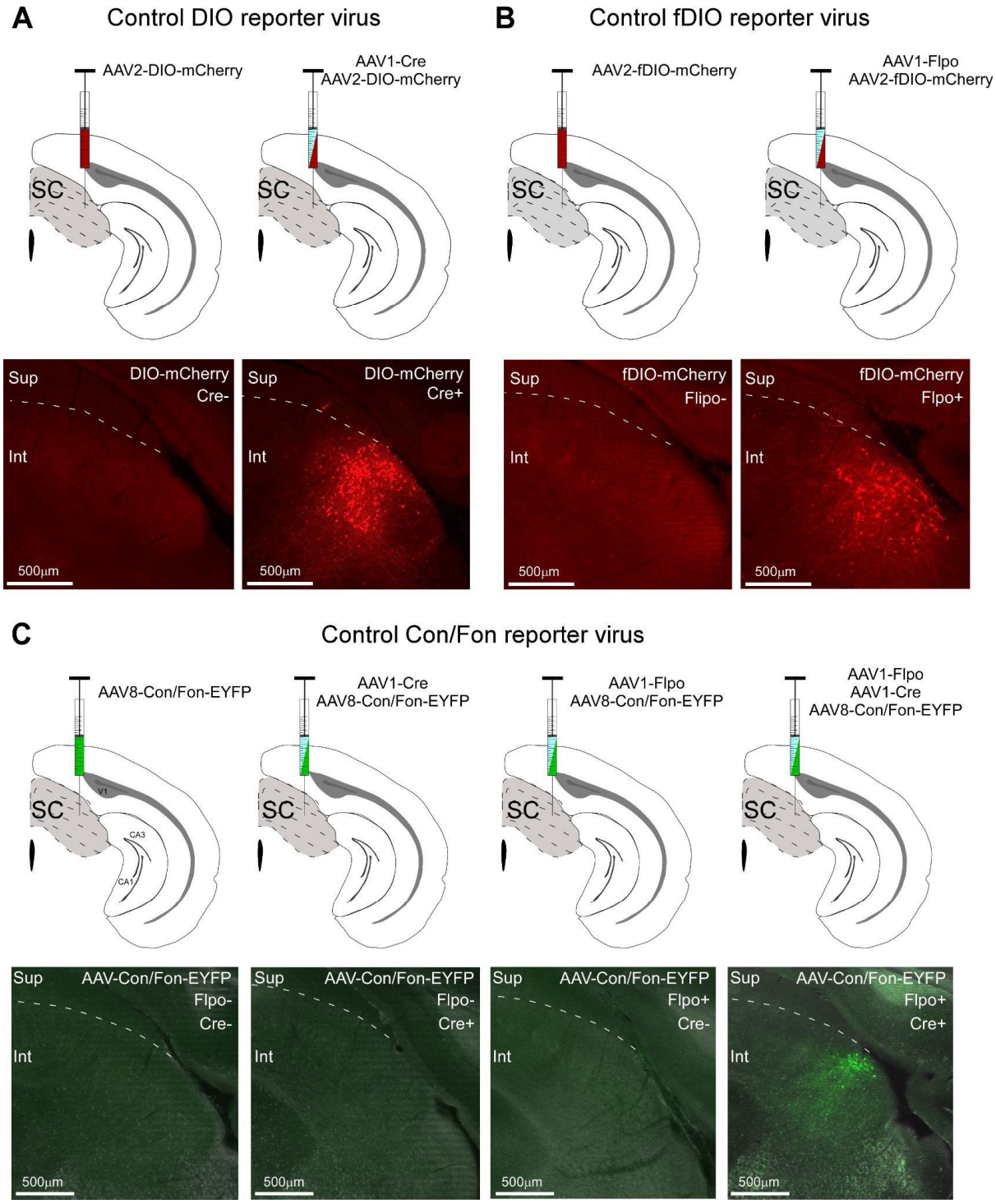


**Fig. S6. Controls for conditional expression of transsynaptic reporter viruses in LSC. Related to Figs. 2-4.**

*(A)* Upper row: Conditional expression of the reporter DIO was tested by injecting AAV2-DIO-mCherry either alone (left) or in combination with AAV1-Cre (right) into the LSC.
Bottom row. Examples of corresponding fluorescence images of the LSC. Conditional expression was only observed in combination with AAV1-Cre (right, red neurons). No leak expression of the reporter virus was detected
*(B)* Same as (*A*) but for Flpo dependent reporter virus. No leak expression of the reporter virus was detected.

*(C)* Upper row: Conditional expression of the reporter virus AAV8-Con/Fon-EYFP was tested by LSC injections of AAV8-Con/Fon-EYFP either alone or in different combinations with transsynaptic viruses: AAV1-Cre and AAV1-Flpo.
Bottom row: Examples of corresponding fluorescence images of the LSC. Conditional expression was only observed for the last combination AAV8-Con/Fon-EYFP & AAV1-Cre & AAV1-Flpo (green neurons); no leak expression of the reporter virus was detected.

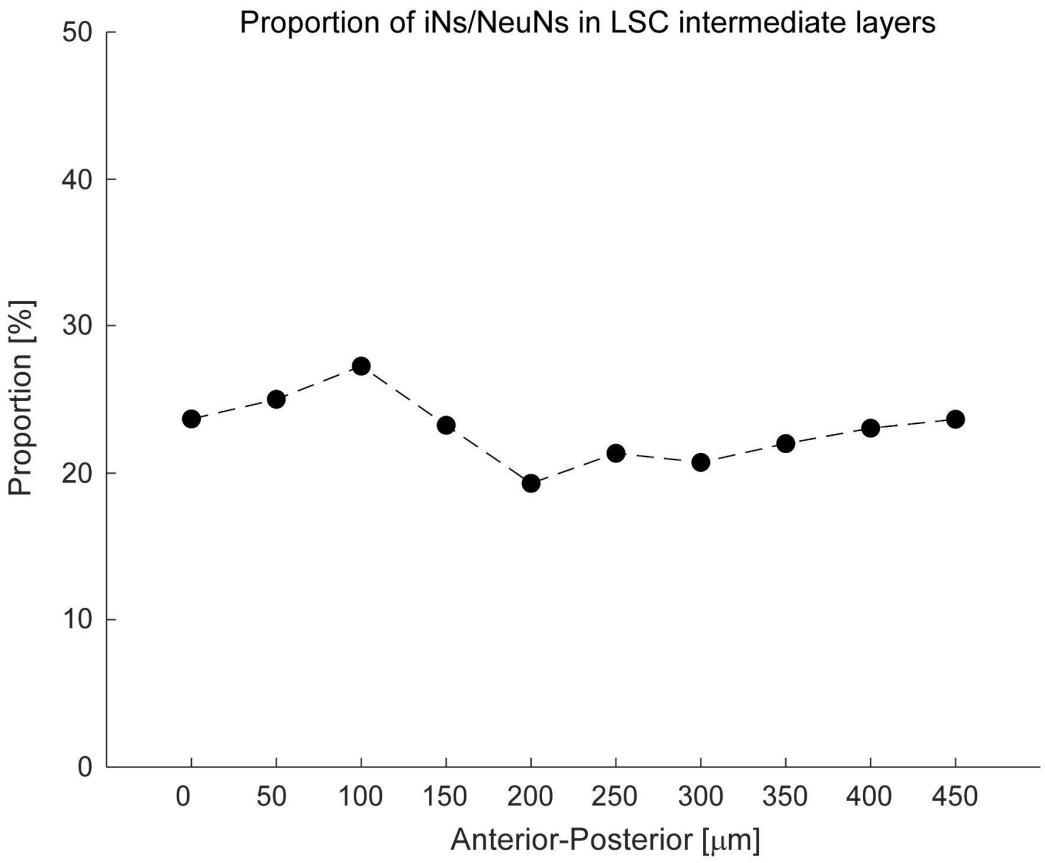


**Fig. S7. Proportion of iNs in intermediate layers of the LSC. Related to Fig.3.**

Proportion of GAD67-GFP positive neurons with respect to immunostained NeuN neurons in the intermediate layer of the LSC. Using a GAD-GFP mouse line, in which GABAergic neurons (iNs) are labeled with GFP, neurons were counterstained with NeuN-Alexa 647 (Fig. 3E). The plot shows the proportion of iNs and NeuN neurons along the anterior-posterior LSC axis.

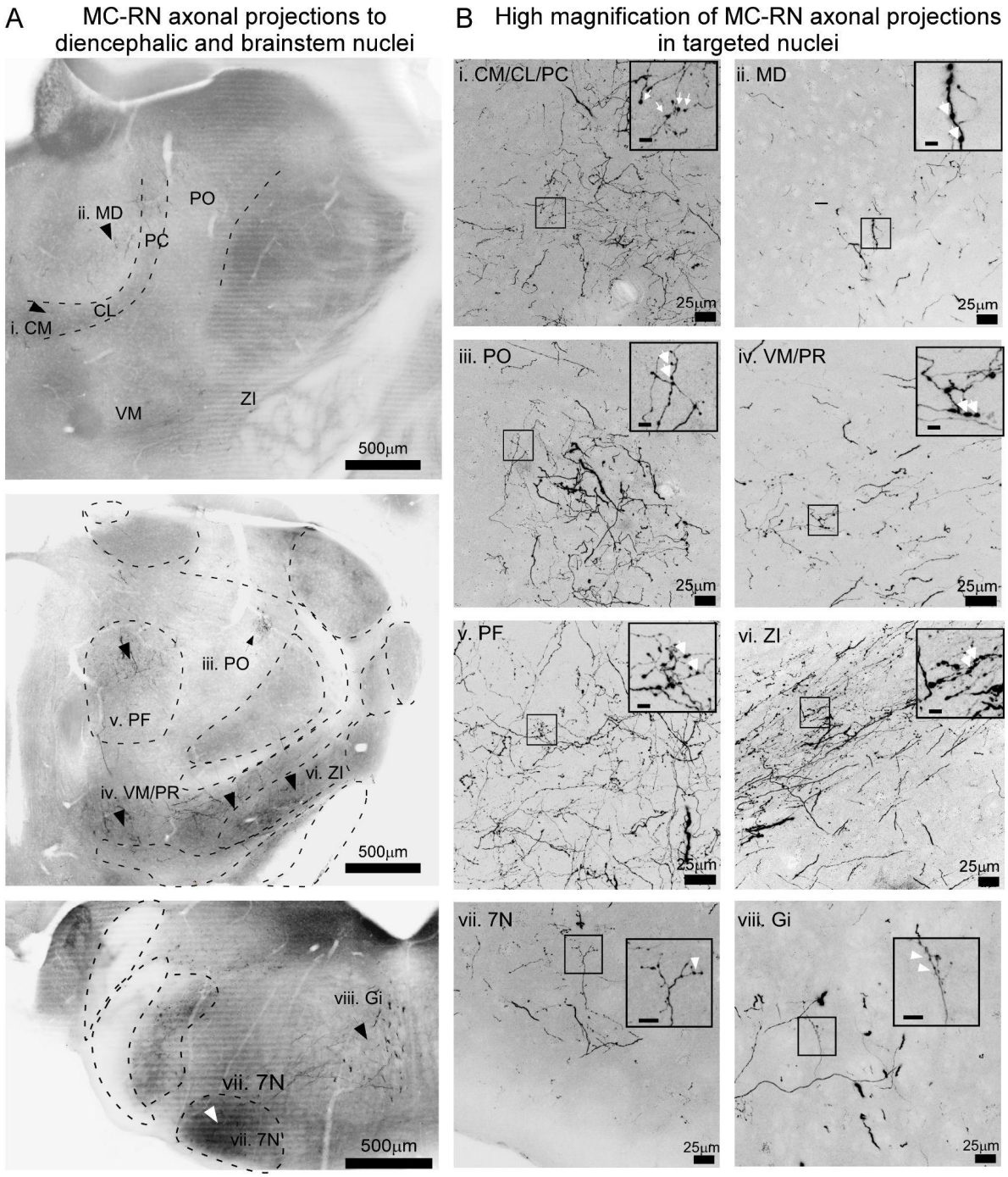


**Fig. S8. Axonal projections and varicosities of MC-RNs in diencephalic and brainstem target nuclei. Related to Fig. 6.**

(A) Desaturated and inverted fluorescence images at two different anterior-posterior coordinates in diencephalic regions (top and middle) and brainstem (bottom), showing MC-RN axons (black arrowheads) at low magnification. Roman numbers enumerate the nuclei shown in *(B)*. Abbreviations: CM, the centro-medial nucleus; CL, centrolateral nucleus; Gi, Gigantocellular reticular nucleus; PC, Precentral; PF; Parafascicular nucleus; PO, Posterior nucleus; nucleus MD, mediodorsal nucleus; VM, ventromedial nucleus; ZI, zona incerta; 7N, Facial nucleus

(B) Confocal images show examples of axons in diencephalic nuclei CM/CL/PC MD, PO, VM, PF, and ZI and in brainstem nuclei, Gi and 7N. Roman numbers indicate the nuclei shown in *(A)*. Small square box indicates the region selected for magnification. Insets show a high magnification of axons and varicosities (white arrowheads), scale bar = 5 μm.

A Trans-collicular inhibitory pathways to higher-order thalamus and zona incerta

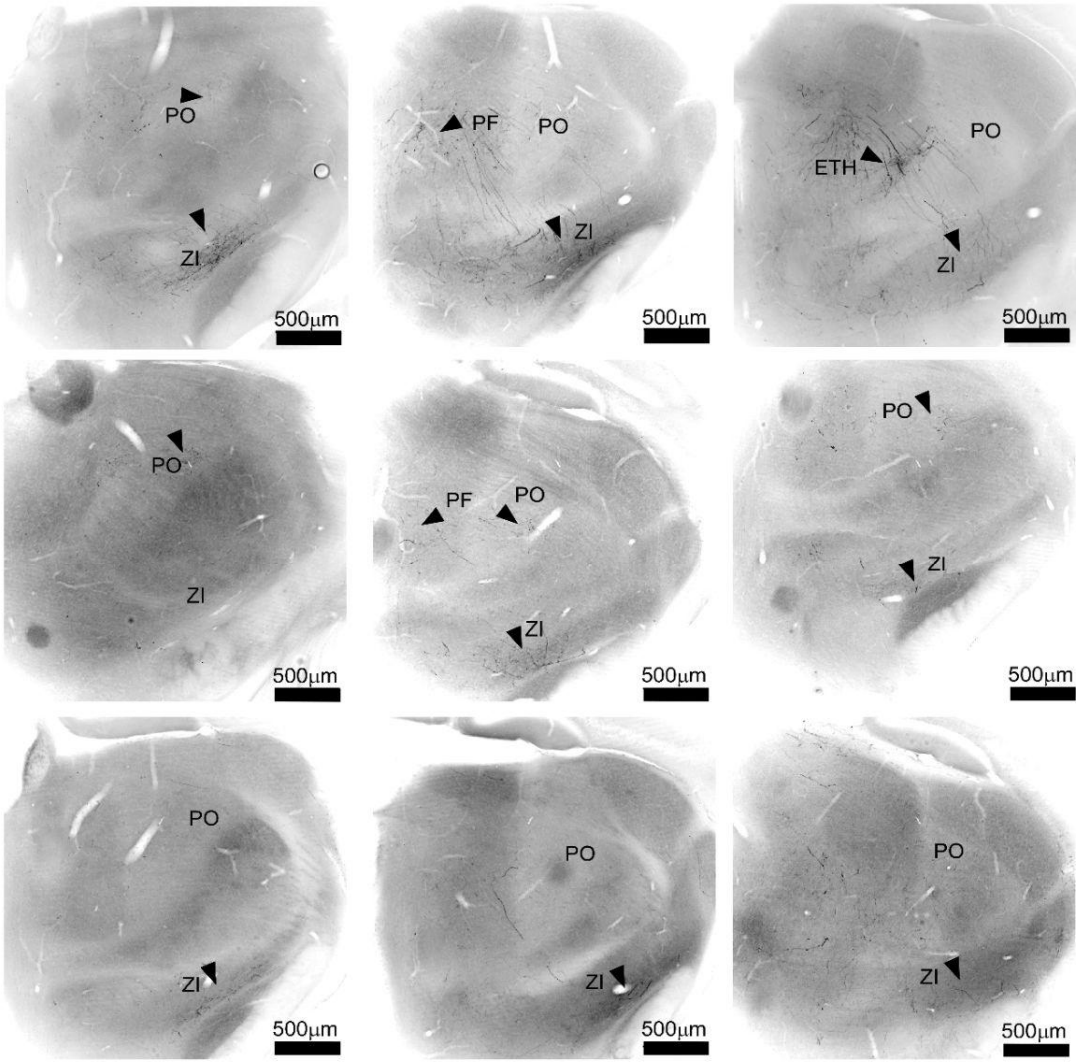


B Example of MC-iRN axons and varicosities in higher-order thalamus and zona incerta

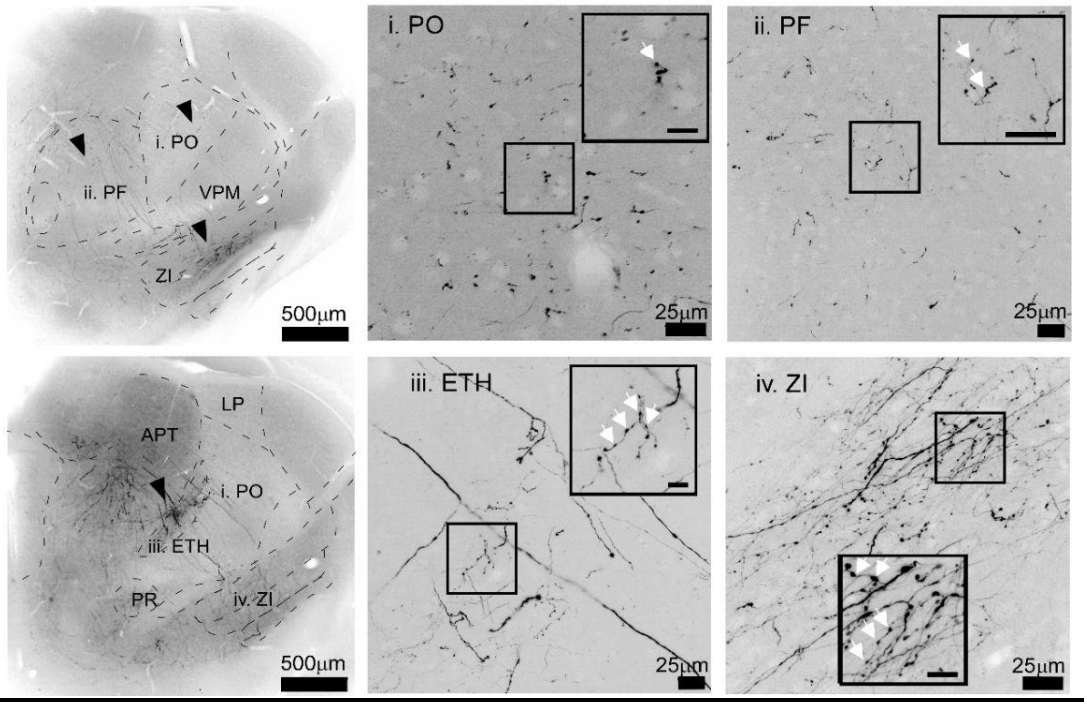

**Fig. S9. LSC-iRN projections to diencephalic regions. Related to Fig. 6.**

*(A)* Desaturated and inverted fluorescence images at three different anterior-posterior coordinates (from left to right) showing MC-, BC-, and Bs-iRNs outputs (top to bottom). Black arrowheads indicate iRN axons. Abbreviations: ETH, Ethmoidal nucleus; Pf, Parafascicular nucleus; PO, Posterior Nucleus; ZI, Zona incerta.

*(B)* Left: Exemplary desaturated and inverted fluorescence images at two different anterior-posterior coordinates showing MC-iRNs outputs in diencephalic nuclei (top and bottom). Black arrowheads indicate axons. Roman numbers enumerate the nuclei shown in high magnification. Abbreviations: APT, Anterior pretectal area; ETH, Ethmoidal nucleus; Pf, Parafascicular nucleus; PO, Posterior nucleus; MD, mediodorsal nucleus; VM, ventromedial nucleus; ZI, zona incerta.

Right: High magnification confocal images show examples of MC-iRN axons in ETH PF, Po, and ZI. Small square box indicates the region selected for magnification Roman numbers indicate the nuclei shown left. Insets show a high magnification of axons and varicosities (white arrowheads), inset scale bar = 10 µm.

| Figure | Comparison | Statistical Test | P value = |
|---|---|---|---|
| 2D | RNs Median location | Kruskal-Wallis | Chi Prob=7.8572e-06 |
| | MC-RNs vs BC-RNs | post-hoc Bonferroni Method | 6.4351e-06 |
| | MC-RNs vs Bs-RNs | post-hoc Bonferroni Method | 0.008951 |
| | BC-RNs vs Bs-RNs | post-hoc Bonferroni Method | 0.061802 |
| 2F Histogram D-V | D-V Cortex vs brainstem Medians | Wilcoxon Rank sum | 0 |
| 2F Histogram M-L | M-L Cortex vs brainstem medians | Wilcoxon Rank sum | 0 |
| 3G | iRN median proportion per slice | Kruskal-Wallis | Chi prob=6.8211e-04 |
| 3G | MC-iRNs vs BC-iRNs | post-hoc Bonferroni Method | 1 |
| | MC-iRNs vs Bs-iRNs | post-hoc Bonferroni Method | 1 |
| | BC-iRNs vs iBs-RNs | post-hoc Bonferroni Method | 1 |
| | MC-iRNs vs iNs | post-hoc Bonferroni Method | 0.0019154 |
| | BC-iRNs vs iNs | post-hoc Bonferroni Method | 0.01571 |
| | Bs-iRNs vs iNs | post-hoc Bonferroni Method | 0.0092727 |
| 4C | CVG-RNs median location | Kruskal-Wallis | Chi prob=8.1595e-10 |
| | Bs&BC vs Bs&MC-RNs | post-hoc Bonferroni Method | 3.3295e-10 |
| | Bs&BC vs BC&MC-RNs | post-hoc Bonferroni Method | 0.00024089 |
| | Bs&MC vs BC&MC-RNs | post-hoc Bonferroni Method | 0.00047532 |
| 4E | CVG-RN median proportion per slice | Kruskal-Wallis | Chi prop=4.2556e-14 |
| | Bs&BC vs Bs&MC-RNs | post-hoc Bonferroni Method | 1 |
| | Bs&BC vs BC&MC-RNs | post-hoc Bonferroni Method | 2.8236e-08 |
| | Bs&MC vs BC&MC-RNs | post-hoc Bonferroni Method | 1.1304e-12 |
| S2B | MC boutons vs BC boutons | Wilcoxon Rank sum | 0.0057 |

**Table S1. Statistical comparisons per figure.**

| Experiment | Neuron Type | N (neuron counts) |
|---|---|---|
| **Retrograde depth profile Fig. 1D** | SC-projecting MC neurons | 71 |
| | SC-projecting BC neurons | 55 |
| **Recipient Neurons (RNs) Fig. 2D** | MC-RNs | 5263 |
| | BC-RNs | 2927 |
| | Bs-RNs | 6702 |
| **Cortical and brainstem inputs Fig. 2F** | Cortica RNs (MC & BC)l, Brainstem RNs | 19179 pixels, 45494 pixels |
| **Inhibitory Neurons (iNs) Fig. 3E** | iNs (Gad-GFP), NeuN | 84, 384 |
| **Inhibitory Neurons (iRNs) Fig. 3E** | iRNs (Cre&Flpo), RNs (Flpo) | 41, 119 |
| **Inhibitory Neurons (iNs) Fig. 3G** | iNs (GAD-GFP), NeuN | 300, 1296 (10 slices, 30 sample sections) |
| **Inhibitory Recipient neurons iRNs, RN Fig.3G** | MC-iRN(Cre&Flpo),MC-RN(Flpo) | 396, 1068 (24 slices) |
| | BC-iRN(Cre&Flpo),BC-RN(Flpo) | 527, 1492 (34 slices) |
| | Bs-iRN(Cre&Flpo), Bs-RN(Flpo) | 1092, 3274 (39 slices) |
| **Convergent Neurons CVG Fig. 4C** | MC&BC-CVG-RN (Cre&Flpo) | 707 |
| | Bs&MC-CVG-RN (Cre&Flpo) | 264 |
| | Bs&BC-CVG-RN (Cre&Flpo) | 115 |
| **Convergent Neurons CVG Fig. 4D** | Cortex&cortex vs<br>Cortex&brainstem | 52 slices<br>65 slices |

| | | |
|---|---|---|
| **Convergent Neurons CVG-RN Fig.4E** | MC&BC-CVG-RN (Cre&Flpo), RN(Flpo) | 636, 2832 (55 slices) |
| | Bs&MC-CVG-RN (Cre&Flpo), RN(Flpo) | 243, 2453 (63 slices) |
| | Bs&BC-CVG-RN (Cre&Flpo), RN(Flpo) | 114, 1391(27 slices) |
| **Gaussian mixture model Fig.4F** | MC&BC-CVG-RN (Cre&Flpo) | 222 |
| **Functional Convergence Fig 5C** | Total Responsive units | 30 |
| | MC-L5→SC responsive units | 25 |
| | BC-L5→SC responsive units | 14 |
| | MC&BC→ SC responsive units | 9 |
| **Bouton diameter FigS2B** | MC→SC boutons<br>BC→SC boutons | 44<br>100 |
| **Whisker SC** | Whisker responsive units | 38 |

**Table S2. Sample sizes per figure.**

| | **Spontaneous firing rate [Hz]** | **Evoked firing rate [Hz]** | **Onset latency [ms]** |
|---|---|---|---|
| **MC-L5 responsive units** | 1.26, 0.71, 2.98 | 111.10, 83.33, 142.36 | 12.68, 11.59, 13.56 |
| **BC-L5 responsive units** | 1.23, 0.96, 4.29 | 95.83, 70.83, 106.25 | 9.51, 8.74, 12.65 |
| **MC-L5 & BC-L5 responsive units** | 1.17, 0.90, 2.45 | MC-L5: 122.92, 78.64, 128.64<br>BC-L5: 95.83, 67.19, 111.63 | MC-L5: 12.24, 11.50, 13.34<br>BC-L5: 9.58, 8.73, 12.64 |
| **Whisker responsive units** | 1.67, 0, 5.83 | 156.2, 70.8 304.2 | 11.80, 6.93, 16.93 |

**Table S3. SC unit population spiking characteristics. Reported values are medians, Q1, and Q3. Related to Fig 5 and S4**